Photonics and Nanostructures - Fundamentals and Applications 58 (2024) 101233

Contents lists available at ScienceDirect

Photonics and Nanostructures - Fundamentals and Applications

journal homepage: www.elsevier.com/locate/photonics

Advances in GeSn alloys for MIR applications☆

V. Reboud [a,*], O. Concepción [b], W. Du [c,d], M. El Kurdi [e], J.M. Hartmann [a], Z. Ikonic [f], S. Assali [g], N. Pauc [g], V. Calvo [g], C. Cardoux [a], E. Kroemer [a], N. Coudurier [a], P. Rodriguez [a], S.-Q. Yu [c,d], D. Buca [b], A. Chelnokov [a]

[a] Univ. Grenoble Alpes, CEA, LETI, 38054 Grenoble, France
[b] Peter Gruenberg Institute 9 (PGI-9), Forschungszentrum Juelich, 52428 Juelich, Germany
[c] Department of Electrical Engineering, University of Arkansas, Fayetteville, Arkansas 72701, USA
[d] Institute for Nanoscience and Engineering, University of Arkansas, Fayetteville, Arkansas 72701, USA
[e] Université Paris-Saclay, CNRS, C2N, 10 boulevard Thomas Gobert, 91120 Palaiseau, France
[f] School of Electronic and Electrical Engineering, University of Leeds, Leeds LS2 9JT, UK
[g] Univ. Grenoble Alpes, CEA, Grenoble INP, IRIG, PHELIQS, 38000 Grenoble, France

ARTICLE INFO

Keywords:
Germanium-tin
Mid-infrared
Photodetectors
Light sources
Group-IV materials

ABSTRACT

Silicon photonics is widely used for near InfraRed (IR) applications up to 1.6 μm. It plays a key role in short-range optical data communications. However, silicon photonics does not really address mid-IR applications, particularly in the 1.6–5 μm wavelength range. This spectral region is essential for environmental/life sensing and safety applications relying on the optical features of molecular vibrations, the aim being to discern and categorize complex chemical entities. Growing markets for such analysis prioritise sensitivity, specificity, compactness, energy-efficient operation and cost effectiveness. The need for a CMOS-compatible integrated photonic platform for the mid-IR is obvious. Such fully-group-IV semiconductor platform should include low-loss guided interconnects, detectors, modulators and, critically, efficient integrated light sources. This paper provides a comprehensive review of recent advances in GeSn-based mid-IR silicon-compatible devices, including optically and electrically pumped lasers, light-emitting diodes and photodetectors. It also discusses the principles underlying these developments, with focuses on material growth techniques and processing methods.

1. Introduction

Silicon photonics, a key technology in optical data communications, has found its place for short-range applications in the near InfraRed (IR) spectrum up to 1.6 μm. It has some potential in emerging fields such as quantum computation, AI and optical signal processing, where complex photonic integration requires the process maturity of high-volume manufacturing. However, silicon photonics does not really address mid-IR applications, particularly in the 1.6–5 μm wavelength range. In this spectral region, applications such as environmental sensing and safety rely heavily on the optical features of molecular vibrations to distinguish intricate chemical entities. These markets continue to grow, driven by the quest for improved sensitivity, specificity, compactness, energy-efficient operation and cost-effectiveness.

Traditional silicon-based integrated circuits (ICs) based on Si CMOS technology have reached their physical limits. Quantum effects, electromagnetic parasitic and process constraints are currently limiting data transmission. To overcome the challenges of purely electrical data transmissions, researchers have proposed to jointly use optoelectronic and microelectronics devices. However, a major drawback has so far

Abbreviations: AFM, Atomic Force Microscopy; CMOS, Complementary metal–oxide–semiconductor; CVD, Chemical Vapor Deposition; CW, Continuous Wave; DHS, Double heterostructure; EL, Electroluminescence; Ge, Germanium; GeSn, Germanium Tin; GR, Growth rate; LED, Light-emitting diode; LH, Light-holes; MQW, Multi quantum wells; Mid-IR, mid-infrared; PD, Photodiode; rms, (Surface) root mean square (roughness); RP-CVD, Reduced Pressure – Chemical Vapor Deposition; RSM, Reciprocal space map; Si, Silicon; SiGeSn, Silicon germanium tin; Sn, Tin; SQW, Single Quantum Well; SRB, Strain-Relaxed Buffers; SSR, Solid-state reaction; TDD, Threading Dislocations Density; TEM, Transmission Electron Microscope; XRD, X-Ray Diffraction.

☆ Special issue on Micro and nano structured mid-IR to Terahertz materials and devices, edited by Mikhail Belkin, Kristinn B. Gylfason, William Whelan–Curtin, Mathias Vanwolleghem and Delphine Marris-Morini.

* Corresponding author.
E-mail address: vincent.reboud@cea.fr (V. Reboud).

https://doi.org/10.1016/j.photonics.2024.101233
Received 25 October 2023; Received in revised form 23 January 2024; Accepted 27 January 2024
Available online 1 February 2024

been the lack of on-chip Si-based light sources. Indeed, current optoelectronic integrated circuits (OEICs) rely on III-V external light sources. While the coupling efficiency between light sources and grating couplers is high, the absence of an on-chip integrated light source limits the use of OEICs.

To overcome this limitation, the focus has shifted to Si-based monolithic OEICs. This approach offers several advantages, including compatibility with mature Si CMOS technology, cost effectiveness, scalability through larger wafer sizes and efficient data transfer through optical interconnections. Si-based monolithic OEICs integrate optoelectronic devices into Si chips, improving chip performance, extending functionality and reducing cost. Despite successful developments in terms of optical waveguides, photodetectors, optical modulators and optical switches, high efficiency light emission in Si-based materials remains challenging due to the indirect bandgap nature of Si, resulting in significantly lower light emission efficiency compared to direct bandgap III-V compound semiconductors. The search for a direct bandgap semiconductor material compatible with the Si CMOS manufacturing process is thus paramount for the fabrication of large-scale Si-based monolithic OEICs.

Integrated mid-IR photonic devices compatible with CMOS technology depend on the development of a fully Group-IV semiconductor platform. It must include interconnects, detectors, modulators and, crucially, efficient light sources integrated on Si in the mid-IR. While Si and Ge are definitely indirect and weakly indirect bandgap semiconductors, respectively, Sn is a semimetal ($E_g(Si) = 1.11$ eV, $E_g(Ge) = 0.66$ eV and $E_g(Sn) = -0.41$ eV). Alloying Ge with Sn results in a faster bandgap reduction at the Γpoint than at the L point of the first Brillouin zone, with the formation of a direct semiconductor for Sn contents above 8% in unstrained GeSn layers. Remarkable progress has been made with Group-IV silicon-germanium-tin (SiGeSn) semiconductors, highlighted by the first GeSn optical cavity laser in 2015, optically pumped room-temperature laser operation in 2022 and electrically pumped GeSn laser cavities in 2020 and 2022. Tensile strain engineering have enabled low Sn content GeSn layers with higher GeSn crystalline quality to become direct bandgap materials. The improvement of device performances is based on (i) the reduction of optical losses, (ii) the use of special growth and etching techniques and (iii) the use of efficient heterostructures.

This review aims to provide valuable insights into ongoing advances in terms of material growth, device fabrication and device concepts related to GeSn and SiGeSn materials. The review is organised to cover various aspects, including epitaxy, strain effects, lasing and optoelectronic devices, while discussing the prospects of integrating these materials into silicon photonic platforms. The overall aim is to provide the reader with a comprehensive understanding of recent experimental advances in the growth of GeSn materials and their uses in optoelectronics.

2. GeSn-based epitaxy for group-IV direct band gap material

Over the past 10 years, optoelectronic components based on germanium (Ge) have been developed to expand the potential of silicon (Si) photonics circuits [1–3]. The main challenge during the epitaxial growth of group-IV materials is the Sn incorporation with large enough concentrations into various individual layers of heterostructures. Sn has a very low solid solubility in Ge and Si and, moreover, possess a very large lattice mismatch with both elements ($a_{Sn} = 6.49$ Å, to be compared with $a_{Si} = 5.43$ Å and $a_{Ge} = 5.66$ Å), making its incorporation into alloys difficult. Furthermore, once deposited, the post-processing temperatures of such alloys are typically limited to the growth temperature of the material, which is relatively low due to the low thermal stability of SiGeSn. This is notably due to differences in terms of melting temperatures between Si (1414 °C), Ge (938 °C) and Sn (232 °C only). Those limitations have a definite impact when aiming for high Sn contents. Far from thermodynamic equilibrium process conditions must then be used, with for instance low temperatures and high growth rates during epitaxy [4–6].

2.1. Intrinsic GeSn growth

Recent advances in non-thermodynamic equilibrium growth techniques enabled to overcome such challenges, resulting in GeSn or SiGeSn alloys with Sn contents definitely higher than their solid solubility limit (0.8% only for Sn in Ge). Among the techniques enabling such epitaxies, Chemical Vapor Deposition (CVD) stands out, with easy-to-use precursors such as Ge_2H_6 or GeH_4 (for Ge), $SnCl_4$ (for Sn) and SiH_4 or Si_2H_6 (for Si) that are very reactive at low temperatures (e.g. in between 275 °C and 375 °C, typically) when mixed. The fabrication of different optical components based on group-IV elements fully compatible with the current Si semiconductor technology such as diodes, detectors, and lasers are proof of the high crystal quality obtained in such CVD-grown materials.

From the viewpoint of optoelectronic devices, high concentrations of Sn (e.g. above 10%) are desired. Indeed, the resulting layers exhibit a strong directness of the energy band structure. These devices also require cladding layers providing optical or electronic confinement, that is, layers with a wider bandgap, which can be achieved with lower Sn concentrations or with the addition of Si. The standard path – as shown by several research groups- is to play with the growth temperature. As seen in Fig. 1a, a decrease of the growth temperature results in an surge of the Sn content in GeSn alloys [7]. However, let us assume that a simple stack like that in the inset of Fig. 1b is required, where a $Ge_{1-x}Sn_x$ layer is deposited on a $Ge_{1-y}Sn_y$ layer, with $x < y$. In that case, the temperature will have to be raised after the deposition of the first $Ge_{1-y}Sn_y$ layer to grow the second $Ge_{1-x}Sn_x$ layer. However, due to the low thermal stability of Sn in Ge, the temperature increase will result in a crystallinity deterioration of the previously grown layer(s), via Sn diffusion or Sn segregation as shown in Fig. 1b.

Different groups have developed alternatives enabling the epitaxial growth of heterostructures with a controlled variation of the Sn content in layers. For instance, Y. Kim *et al.* [8] and M. R. M. Atalla *et al.* [9] took the risk of controlling the Sn content in the different layers through small changes in the growth temperature (less than 10 degrees) during the fabrication of photodetectors and strain-free GeSn microdisk laser devices (Fig. 2a). With this, variations of around 2% of the Sn content were achieved without layer degradation or Sn segregation. However, as explained above, larger changes in temperature are not feasible and a variation of only 2% Sn is small for the fabrication of optoelectronic devices. J. Aubin *et al.* [10] on the other hand, used a more conservative path. Without any change in the growth temperature, they achieve Sn variations of up to around 4% thanks to $SnCl_4$ precursor flow changes (Fig. 2b). The same group used both approaches (e.g. temperature and $SnCl_4$ changes) to fabricate room temperature (RT) optically pumped GeSn microdisk lasers with an active region made of $Ge_{0.868}Sn_{0.172}$ [11]. To do that, they gradually reduced the growth temperature from 349 °C down to 307 °C until a Sn content of 17.2% in the active region was reached. Then, without increasing the temperature, they went back to 14.1% in GeSn layers on top, thanks to a reduction of the $SnCl_4$ flow. With this approach, this group decreased the threat of having Sn surface segregation and precipitation (Fig. 2b).

Recently, O. Concepción *et al.* [12] proposed a new path for Sn control. Without changing the growth temperature or the precursors flow, they succeeded in changing the Sn content by up to 6%, thanks to N_2 carrier gas flow changes (Fig. 2c). The partial pressure of the precursors increased proportionally with the decrease of the N_2 flow in the reactor. As a direct consequence, the gas velocity decreased, that is, the duration for which reactive precursors remain in the reactor increased, resulting in a rise of the content of Sn in alloys. The relevance of this approach was demonstrated at different growth temperatures, with the same behaviour obtained. Such a strategy was successfully used for the growth of different isothermal heterostructures for vertical MOSFET

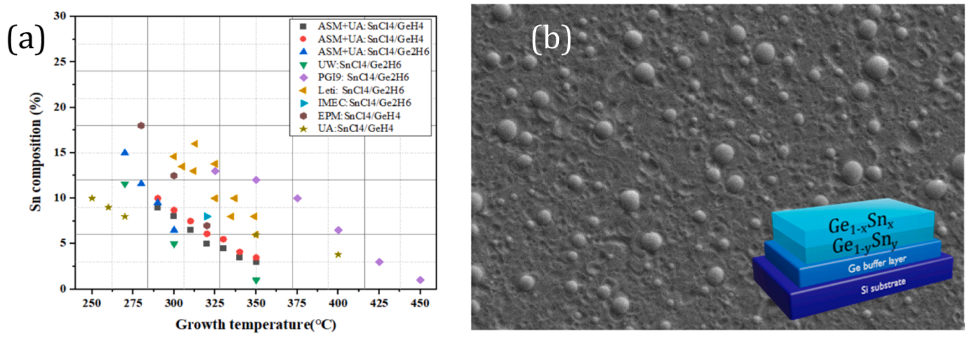

Fig. 1. (a) Impact of growth temperature on Sn content as reported by different research groups. A clear increase of the Sn content into the GeSn alloys is obtained thanks to a temperature decrease. (b) SEM image showing Sn segregation. Inset: sketch of a hypothetic $Ge_{1-x}Sn_x/Ge_{1-y}Sn_y$ heterostructure with $x < y$. Reproduced from [7].

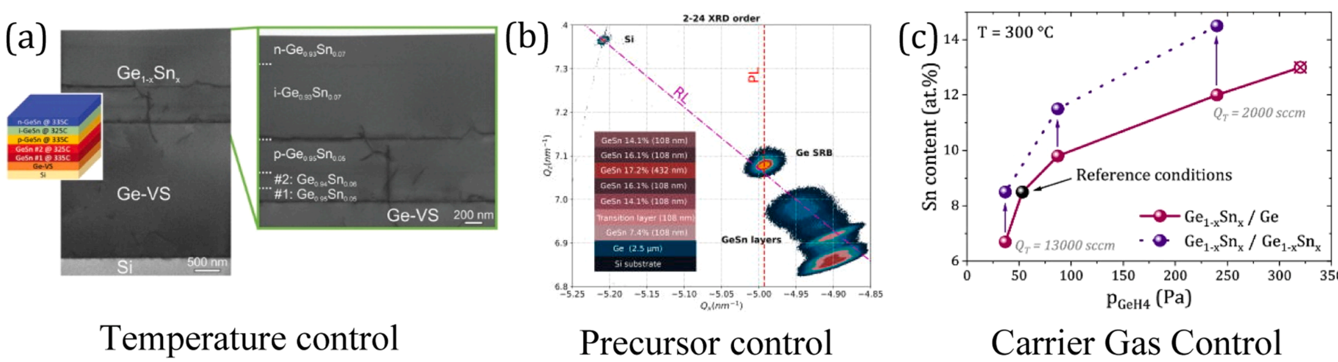

Fig. 2. Control of the Sn content into heterostructures through changes in the (a) process temperature, (b) temperature and $SnCl_4$ flow, and (c) N_2 carrier gas flow. Reproduced from [8,10] and [12].

devices, CMOS invertors, tunnelling field-effect transistors and multiple quantum well designs for GeSn light sources in which abrupt interfaces with well-defined Sn contents were obtained.

2.2. *Doped GeSn growth*

2.2.1. *In-situ GeSn doping*

Doping plays a crucial role in enhancing the performance of semiconductor materials and optoelectronic devices. The in-situ doping of GeSn and SiGeSn for use in complex GeSn/SiGeSn p-i-n heterostructures was thoroughly assessed in Refs. [13,14]. $Ge_2H_6 + Si_2H_6 + SnCl_4 + PH_3$ or B_2H_6 chemistries were used, at 350 °C, 100 Torr, for the n-type or p-type doping of GeSn and SiGeSn layers. A Sn concentration drop, from ~ 6.5% in intrinsic layers, down to 6.0% or 4.9% was evidenced in GeSn: P or GeSn:B layers as the PH_3 or B_2H_6 flow increased. Meanwhile, there was a slight GeSn:P increase and a substantial GeSn:B growth rate increase, from ~ 40 up to 43 and from ~ 40 up to 53 nm min.$^{-1}$, as the dopant flow increased (Fig. 3a). The B concentration increased monotonously as the B_2H_6 flow increased, from a few 10^{17} cm^{-3} up to ~ 5×10^{19} cm^{-3}, the vast majority of B atoms being electrically active (Fig. 3b). The atomic P concentration also increased monotonously with the PH_3 flow, from 3×10^{19} cm^{-3} up to 4×10^{20} cm^{-3}. There was however a saturation at 7×10^{19} cm^{-3} then a decrease down to 4×10^{19} cm^{-3} of the P^+ ion concentration, probably due to the creation of electrically inactive Sn_mP_n-V clusters (Fig. 3c).

Adding Si_2H_6 to the same Ge_2H_6 and $SnCl_4$ flows as in GeSn resulted in the following. First, as the PH_3 flow increased, the Si concentration in SiGeSn:P layers remained close to 14% while the Sn concentration slightly increased from 8% up to 10%. Meanwhile, the Si concentration in SiGeSn:B layers definitely raised with the B_2H_6 flow, from 14% up to 25%, while the Sn concentration dropped, from 9% down to 7%. Such ternary alloy composition changes were associated with slight SiGeSn:B growth rate increases and SiGeSn:P growth rate decreases as the dopant flow increased, from ~ 30 up to 34 and from ~ 30 down to 27 nm min^{-1}, respectively (Fig. 3a). The presence of significant amounts of Si in GeSn boosted, for given dopant flows, the B or P concentrations in SiGeSn compared to those in GeSn. More than 2×10^{20} cm^{-3} and 3×10^{20} cm^{-3} B and P ions concentrations were achieved in SiGeSn:B and SiGeSn:P, respectively, with apparently a lack of electrically inactive Sn_mP_n-V clusters, as P ions concentrations were then close to P atomic concentrations (Fig. 3b and Fig. 3c).

2.2.2. *Ex-situ GeSn doping*

Ex-situ ion implantation, followed by a subsequent annealing step for dopant activation and layer recrystallization, can be used to dope GeSn [15]. Ex-situ doping is a widely used method in microelectronics as it enables localised implantation. It is otherwise compatible with various process flows. One of the main challenges in the case of GeSn is to activate dopants, which requires temperatures above the epitaxial growth temperature. Researchers investigated the ex-situ doping of both Ge and GeSn using rear side flashlamp annealing (r-FLA) [16,17]. r-FLA resulted in the formation of less defective doped layers in comparison of front-FLA [17].

The influence of nanosecond laser annealing (NLA) on thick GeSn layers that were implanted with phosphorous ions and on poly-GeSn was assessed in Refs. [18,19], respectively. UV-NLA, thanks to its extremely brief pulse duration and its short wavelength, yields high temperatures near the surface of the absorbing material, while keeping the buried layers at lower temperatures. This is particularly useful for GeSn layers which have a low thermal stability. NLA was recently used to achieved elevated effective carrier concentrations within the polycrystalline GeSn or create low resistance contacts on GeSn [19,20]. Thick $Ge_{0.92}Sn_{0.08}$ layers implanted with phosphorus ions were used as test structures to evaluate the crystalline quality, strain and tin distribution of

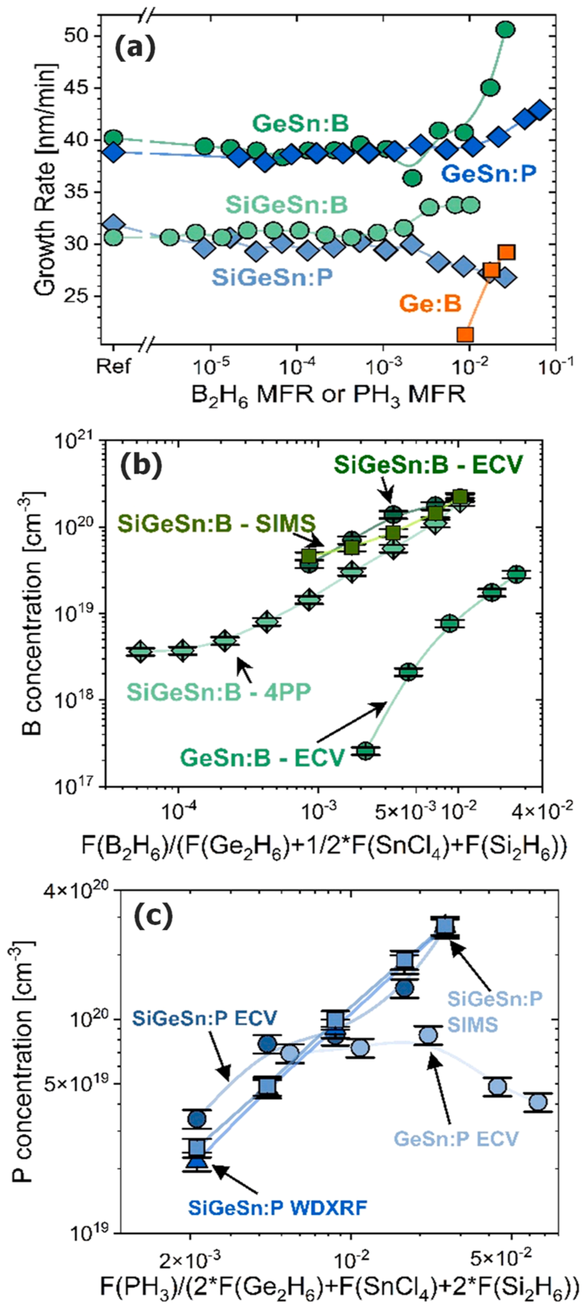

Fig. 3. (a) GeSn:B, GeSn:P, SiGeSn:B and SiGeSn:P growth rates @ 350 °C, 100 Torr as functions of the B_2H_6 or PH_3 Mass-Flow Ratios. (b) B ions concentrations from 4 points probe (4PP) measurements or electrochemical capacitance voltage (ECV) depth profilings together with B atomic concentrations from Secondary Ions Mass Spectrometry (SIMS) in pseudomorphic (Si) GeSn:B layers grown at 100 Torr and at 350 °C, on Ge SRBs, themselves on Si (001) substrates. (c) P ions concentrations in pseudomorphic (Si)GeSn:P layers grown at 100 Torr and at 350 °C, on Ge SRBs from 4PP or ECV together with P atomic concentrations from SIMS. Constant Ge_2H_6, $SnCl_4$ and Si_2H_6 flows. Reproduced from [14].

recrystallised GeSn layers after UV-NLA, with results superior to that with traditional rapid thermal annealing (RTA) [18].

2.3. GeSn/SiGeSn MQW growth

As discussed previously, it is nowadays well known that the growth of GeSn/SiGeSn stacks on Si substrates is challenging due to the large lattice mismatch with Si (> 4.2%) and the low solubility (< 1%) of Sn in Ge, the instability of α-Sn above 13 °C, and. Thanks to ground-breaking research on non-equilibrium condition growth techniques, stacks deposited with MBE or CVD with Sn contents far beyond 1% are nowadays a reality [21–25].

2.3.1. Growth and structural characterization of single quantum wells

Multi-Quantum Wells (MQWs), despite being highly suitable for devices, pose challenges in exploring their optical properties, potentially due to their inhomogeneous structures. Performing comprehensive studies on Single Quantum Wells (SQWs), with a focus on material growth, optical transitions, recombination mechanisms and band diagram modelling should give clear guidances for next future MQW-based device designs.

Fig. 4a shows SIMS depth profilings of Sn and Si in a SQW sample grown in an industrial standard RPCVD reactor with cost-efficient, commercially available Si, Ge, and Sn precursors [26]. The Ge buffer layers were grown using a two-step growth technic using 10% GeH_4 in purified H_2: a ~150 nm seed layer was grown at T < 400 °C with a H_2 carrier. Subsequently, the remaining approximately 550 nm were grown at 600 °C. A post-growth in-situ anneal was performed at T > 800 °C to minimize the amount of defects. The temperature of the chamber was then reduced down to T < 400 °C in H_2. After which, the SiGeSn/GeSn stack was grown using GeH_4, SiH_4, and $SnCl_4$ precursors in the chamber [9]. SnCl4, a liquid at room temperature, is delivered using a bubbler held at RT, where H_2 gas is metered to regulate the mass flow of $SnCl_4$. A piezoelectric acoustic sensor was utilized to measure the mass flow of $SnCl_4$ downstream of the bubbler. The signal was looped back to the H_2 bubbler mass flow controller (MFC) in a dynamic control loop, enabling continuous monitoring and adjustment of the $SnCl_4$ mass flow to maintain the desired set-point. The complete structure included (i) a 700-nm-thick Ge buffer, (ii) a nominally 600-nm-thick $Ge_{0.914}Sn_{0.086}$ buffer, and (iii) a 9-nm-thick $Ge_{0.87}Sn_{0.13}$ well sandwiched in-between a 78-nm-thick $Si_{0.042}Ge_{0.892}Sn_{0.066}$ bottom barrier and a 54-nm-thick $Si_{0.036}Ge_{0.897}Sn_{0.067}$ top barrier. The compositions of Sn in the buffer, bottom barrier, well, and top barrier were measured at 8.6%, 6.6%, 13.0%, and 6.7%, respectively. Meanwhile, the Si compositions in the bottom and top barriers were determined to be 4.2% and 3.6%, respectively.

A High Resolution X-Ray Diffraction (HRXRD) 2θ-ω scan is presented in Fig. 4b. The peak at 66.07° corresponds to the one of Ge buffer. Peaks at 64.02° and 64.94° are correspond to the $Ge_{0.87}Sn_{0.13}$ well and $Ge_{0.914}Sn_{0.086}$ buffer, respectively. The peaks corresponding to the SiGeSn bottom and top barriers were observed at 65.54°. The peaks overlapped due to the proximity of Si and Sn compositions in the bottom and top barriers.

Because of the quantum-size effect, the ground energy level is in the well exists above the minimum of the Γ valley in its bulk counterpart, resulting in a reduced effective barrier height. Growing a thicker well should lower the ground energy level and thus improve carrier confinement. Fig. 5a shows SIMS depth profile of another SQW with very similar Sn and Si concentrations but with a 22-nm GeSn well thickness [27].

Sn compositions are indeed 6.4%, 13.5%, 6.3%, and 8.6% in the SiGeSn top barrier, the GeSn well, the SiGeSn bottom barrier and the GeSn buffer, respectively. HRXRD 2θ-ω scans on that second SQW are shown in Fig. 5b. The black curves represent the measured data, while the red curves depict the simulation results. The peak observed at 66.1° is linked to the Ge buffer. Peaks at 63.8° and 64.8° are assigned to the GeSn well and the GeSn buffer, respectively. The peak at 65.4° is due to the SiGeSn barriers. As Si and Sn compositions are close in the top and bottom barriers, peaks are overlapped. XRD simulations yielded 64, 22, and 70 nm thicknesses for the SiGeSn top barrier, the GeSn well, and SiGeSn bottom barrier, respectively. Such thicknesses were in line with SIMS profiles shown in Fig. 4a. The two small peaks near the 65.4 ° peak are Pendellösung fringes. Their presence highlights the high quality of the SQW regarding its uniform composition and smooth interfaces.

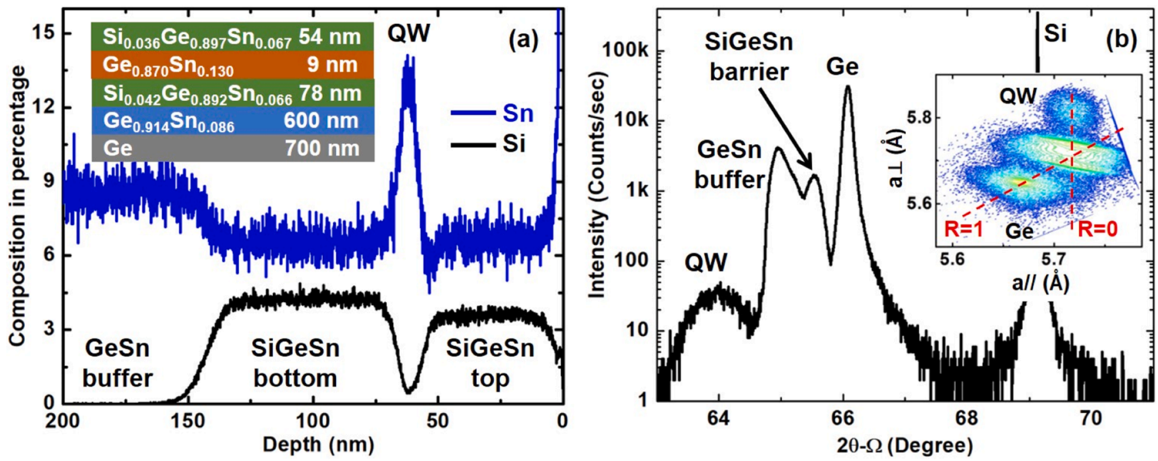

Fig. 4. (a) SIMS displaying each layer thickness and Si and Sn compositions. Inset: Schematic of the SQW structure; (b) XRD 2θ-ω scan presenting each resolved peak. Inset: RSM contour plot.
Reproduced from [26].

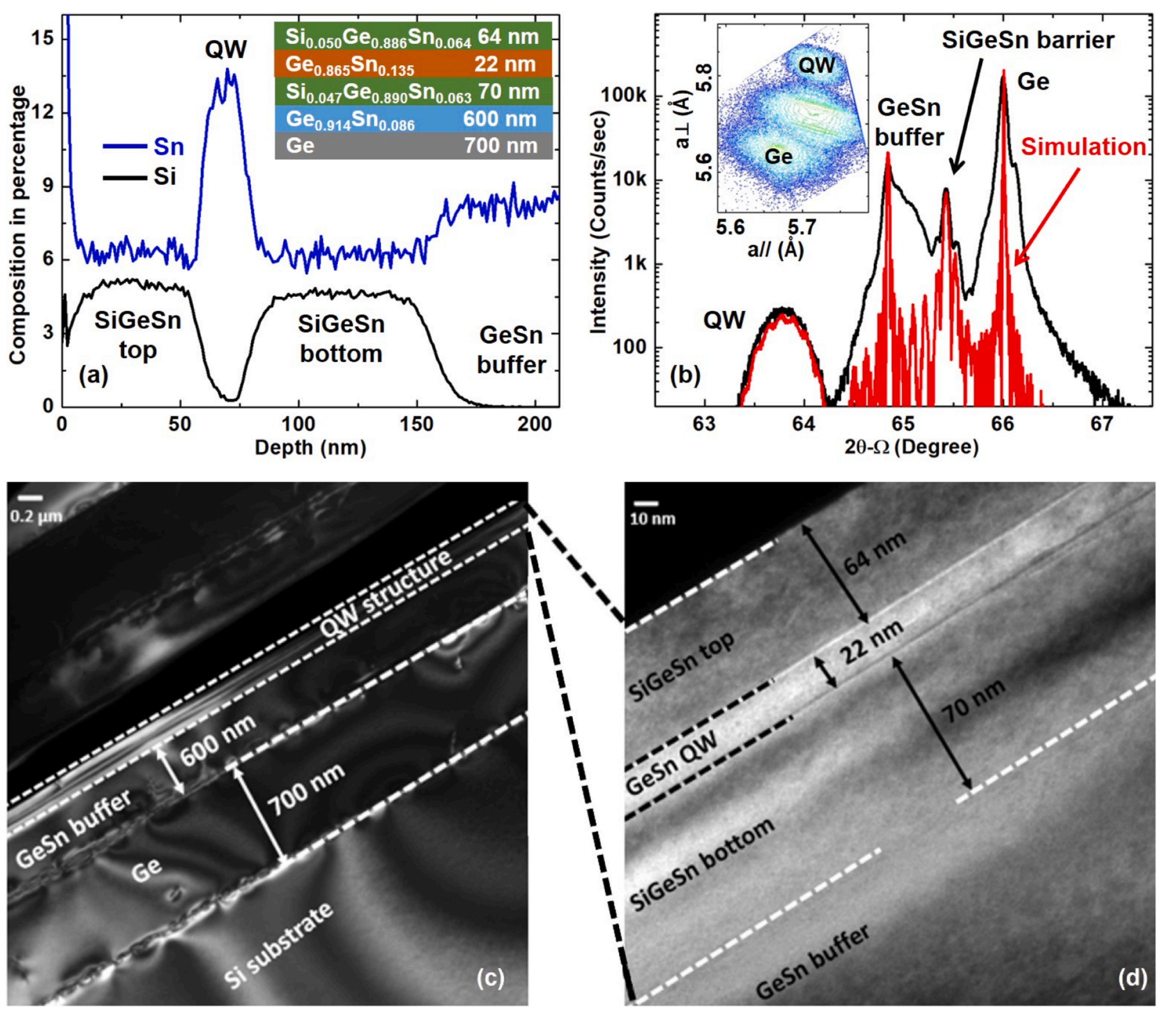

Fig. 5. (a) SIMS depth profiles of Si and Sn in SQW; Inset: cross-sectional schematic of that second SQW. (b) HRXRD 2θ-ω scan presenting each resolved peak. The measured data is represented by the black curve, while the simulation results are depicted by the red curve. Inset: (224) RSM contour plot. (c) Cross-sectional TEM image showing each layer. (d) TEM image showing detailed QW structure.
Reproduced from [27].

Fig. 5c shows a cross-sectional Transmission Electron Microscopy (TEM) image of this second SQW. Misfit dislocations are localized at the Ge/GeSn buffer interface and do not propagate towards to the SQW region, resulting in high crystalline quality material. A focus on the SQW structure is shown in Fig. 5d. Every layer is clearly resolved, with abrupt interfaces and a lack of extended defects. Layer thicknesses are otherwise in line with SIMS and XRD results.

2.3.2. Growth and structural properties of multiple quantum wells

MQW samples were grown in the same industrial RPCVD tool than SQWs. Prior to MQW growth, a nominally 900-nm-thick $Ge_{1-x}Sn_x$ buffer was grown with a graded Sn composition from 6% to 9%. Our aim was to minimize the compressive strain in $Ge_{1-x}Sn_x$ wells and obtain bandgap directness. MQWs were then grown pseudomorphically on the relaxed GeSn buffers.

Fig. 6a shows a typical SIMS depth profile of Sn and Si in a MQW sample with 6 wells [28]. The Sn compositions in the wells and barriers were of 12.5% and 10.0%, respectively. The thicknesses of the well and barriers were determined to be 12 and 4 nanometers, respectively. 2% of Si and 9% of Sn were present in the SiGeSn barriers. Fig. 6b shows a cross-sectional TEM image of that MQW. The defect density is low in the $Ge_{1-x}Sn_x$ buffer, enabling high-quality MQW growth. Moreover, layer thicknesses from TEM were in line with what was intended, indicating a good control of material growth.

A HRXRD 2θ-ω scan is plotted in Fig. 6c. The broad peak adjacent to the Ge peak at ~65° is due to:

(i) the $Ge_{1-x}Sn_x$ buffer; as the Sn composition in the $Ge_{1-x}Sn_x$ buffer gradually increased from 6 to 9%, the peak is broad;.

(ii) $Si_{0.02}Ge_{0.92}Sn_{0.06}$ barriers. Incorporating Sn caused a shift of the peak to a lower angle, whereas the addition of Si resulted in the opposite effect, producing a higher-angle shoulder on that peak.

(iii) $Si_{0.02}Ge_{0.89}Sn_{0.09}$ bottom barrier. This peak should be overlapped with the broad peak given the Si and Sn compositions.

Peaks at ~64.2° and ~63.2° are due to $Ge_{1-x}Sn_x$ barriers and wells, respectively.

A Reciprocal Space Map around the (224) XRD order is shown in Fig. 6d. R= 0 and R= 1 lines are full relaxation and pseudomorphic lines, respectively. Both the Ge and $Ge_{1-x}Sn_x$ buffer layers exhibit nearly relaxed states with residual tensile strains of 0.18% and 0.16%, respectively. Since the MQW stack was grown pseudomorphically on the $Ge_{1-x}Sn_x$ buffer, the SiGeSn bottom and top barriers display a compressive strain of 0.10%, whereas the $Ge_{1-x}Sn_x$ barrier and well are under higher compressive strains, measured at 0.75% and 1.25%, respectively.

3. Room temperature optically pumped lasers

Following the initial demonstration of optically-pumped lasing in GeSn in 2015 [29], there were subsequent breakthroughs, including achieving electrically-injected lasing up to 90 K in ridge waveguides [30] or up to 90 K in microrings [31] and continuous wave (CW) laser operation up to 70 K [32]. Up to quite recently, however, GeSn lasing was limited by (i) the presence of defects, (ii) a lack of optimized design for optical confinement and (iii) thermal management issues, resulting in lasing thresholds in the range of MW/cm^2 above 100 K. An important milestone towards real-field applications is however the ability to

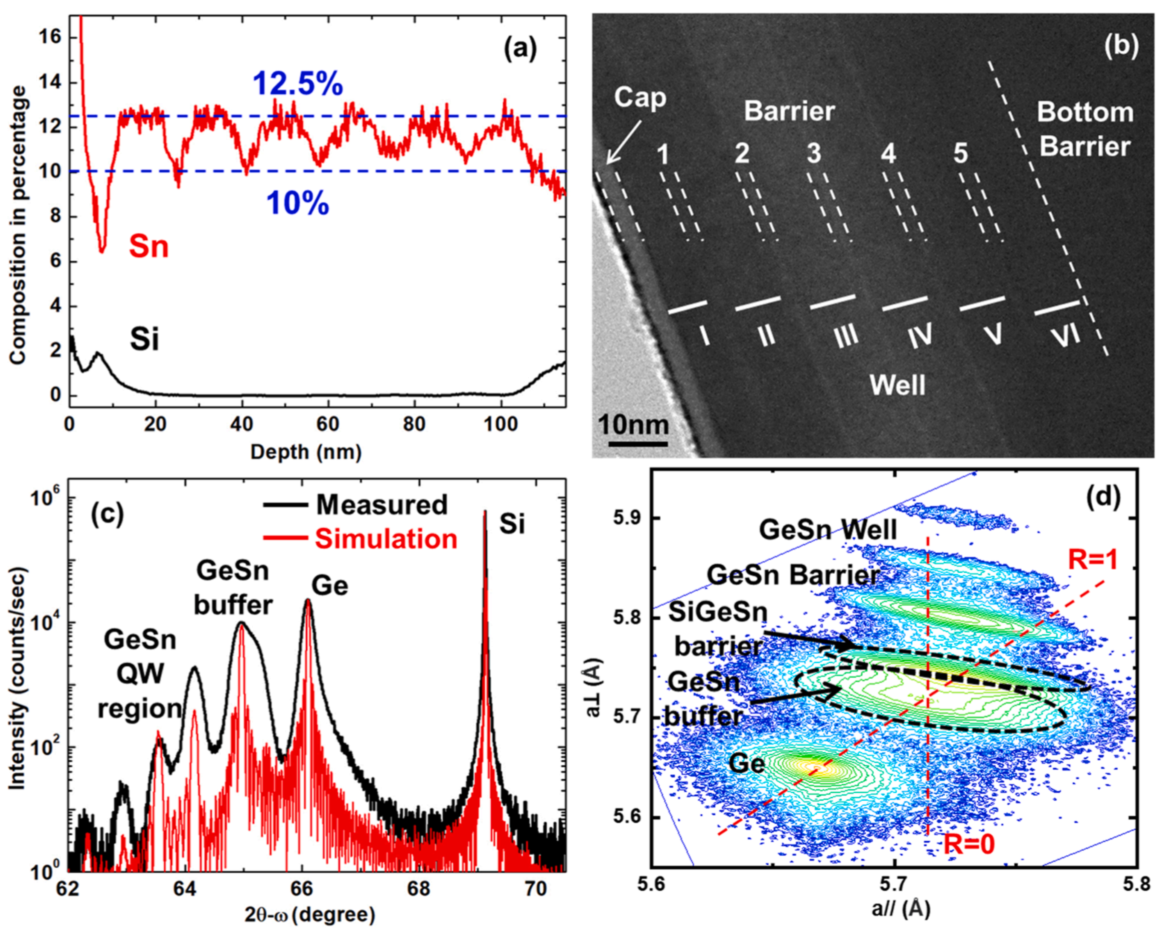

Fig. 6. (a) SIMS depth profiles of the Si and Sn content in the MQW; (b) Cross-sectional TEM image of that MQW; (c) Measured (black) and simulated (red) HRXRD 2θ-ω scan; (d) RSM contour plot around the (224) XRD order.
Reproduced from [28].

operate at RT. Up to 2021, the highest temperatures reported for optically-pumped laser operation were 273 K for 16% of Sn and 270 K for 15% to 20% of Sn, although bandgap directness was expected to be high enough to reach RT lasing [11,30]. We review in this section the latest progress on optically-pumped GeSn cavities [5,33,34] operating at room temperature.

A critical parameter to have a performant laser at high temperature is indeed the directness of the band structure, which is defined as the energy barrier between the zone center (Γ) and the indirect valleys (L) of the conduction band. Usually, this barrier energy is within the range of 150–200 meV, to have a meaningful Γ-state electron population up to RT and an optical gain at direct transitions with the valence band hole states. To reach such a bandgap directness, a high amount of tin in strain-relaxed alloys is required, of the order of 16%. Achieving such elevated tin contents poses a significant challenge due to the solubility limit of Sn in Ge and the large lattice mismatch with Si substrates, as discussed in Section 1. In practice, employing of Ge SRBs was shown to be most appropriate for the growth of GeSn alloys, as it mitigated the large lattice mismatch with Si substrates. Increasing the Sn content in GeSn layers grown on Ge SRBs results in a large compressive strain that reduces the band gap directness and degrades the gain. The prevalent method to address challenges related to compressive strain for pseudomorphic GeSn layers on Ge, involves deliberately surpassing the critical thickness of layer growth, leading to approximately 70% plastic strain relaxation. This process yields dense arrays of misfit dislocations close to the GeSn/Ge SRB interface, leading to non-radiative carrier recombination that hampers lasing efficiency.

In a previous work, a different path has been proposed, relying on tensile strain engineering [76] in order to have a higher degree of freedom in terms of band structure engineering and gain optimization. From the practical point of view, only a few groups were able to inject some tensile strain in GeSn alloys resonator for lasing. It typically requires suspended active GeSn regions, with thermal management issues, however [35]. A new platform relying on GeSnOI technology has been proposed, using dielectric layers as claddings. Such a platform offers many advantages with respect to more conventional approaches explored so far. The main assets of this platform are threefold:

- a removal of GeSn/Ge SRB interfacial defects through an etching of the buried Ge/GeSn interfacial region after the bonding of the stack on the carrier Si sample;.

- enhanced optical confinement is achieved compared to conventional GeSn/Ge SRB stacks thanks to the higher optical index contrast between GeSn and the cladding;.

- the strain transfer enables a higher bandgap directness of alloys with the use of SiN stressors as dielectric cladding layers.

Such an approach yielded one of the first two room temperature lasing operation, as detailed below, and the first continuous wave lasing with GeSn.

The GeSnOI technology offers many design possibilities. It is a versatile approach which can be applied for various types of gain media, e.g. with different Sn contents, or heterostructures.

3.1. GeSnOI laser cavities design and fabrication

Fig. 7: presents a flow to fabricate GeSn on insulators. The process starts with the growth of a thick GeSn layer (Fig. 7:a) followed by the deposition SiN stressor and multilayers (Fig. 7:b). A thick Au layer can be deposited on a host Si substrate. The two samples are bonded using Au-Au thermo-compressive bonding at 300 °C (Fig. 7:c). After removal of Si used to grow GeSn and the Ge SRBs (Fig. 7:d), the substrate is patterned using conventional lithographic steps (Fig. 7:e). The GeSn micro-disk is then liberated by based deep reactive ion etching (DRIE) (Fig. 7:f and g) and can be encapsulated with a second SiN stressor (Fig. 7:h).

In Fig. 8a and Fig. 8b, a GeSnOI stack using a SiN dielectric layer as cladding is shown. The underlying aluminum layer functions as a heat sink, while the SiN layer serves as a stressor and facilitates optical confinement. After bonding, the Si substrate was removed by selective etching with respect to the Ge SRB thanks to a diluted KOH solution. A dry etching step was utilized to eliminate the Ge SRB and defects at the GeSn/Ge interface using a SF_6 plasma in an ICP (Inductively Coupled Plasma) etching tool. Subsequently, the initial GeSn layer was reduced from its as-grown thickness of 500 nm to 400 nm to get rid of the defective interfacial layer, which was then on top. The crystalline quality was improved, which resulted in an improved carrier injection efficiency. The GeSn/SiN optical index contrast reached a level sufficient to offer good optical confinement for both TE and TM polarized modes: overlap factors were 93% for TE and 77% for TM, e.g. values very close to that with suspended GeSn microdisks in the air. Microdisk cavities with a mesa shape were fabricated, without the need for additional optical confinement via under-etching. Such resonators were bonded on the aluminium thermal dissipator underneath, as shown in Fig. 9b, with an improved heat flux towards the substrate. A detailed comparison between GeSnOI microdisk mesa and suspended GeSn/Ge

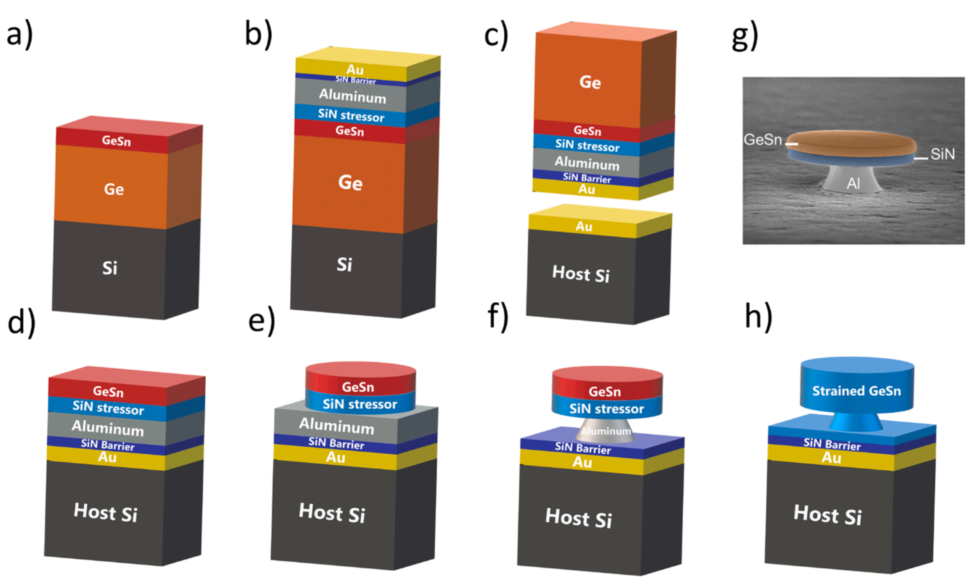

Fig. 7. Example of process flow to fabricate GeSnOI and to strained GeSn micro-disks.

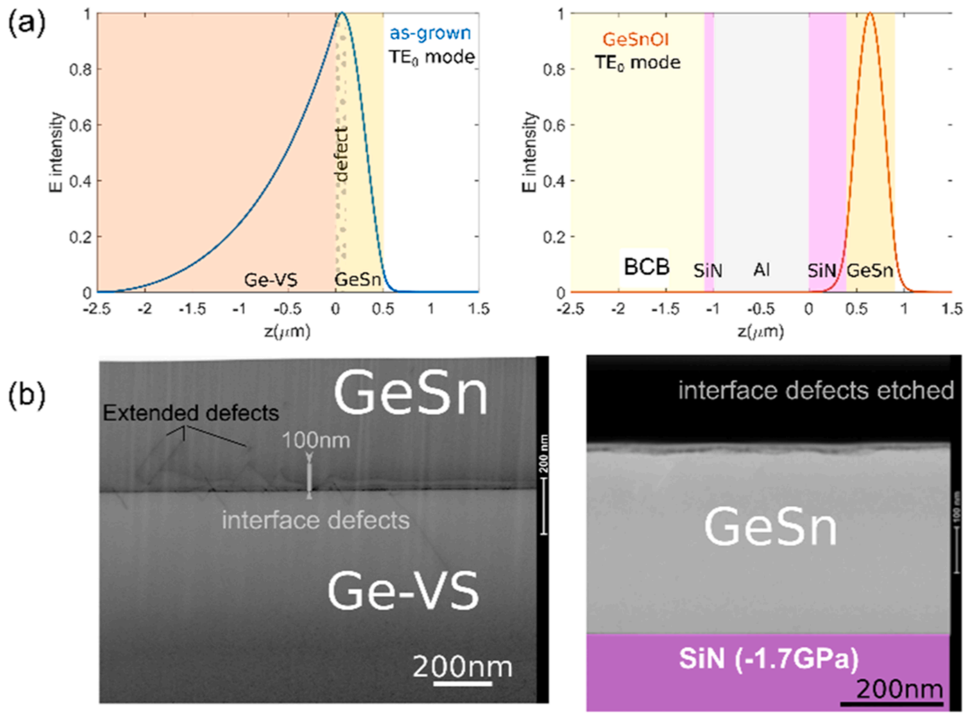

Fig. 8. (a) Electric field intensity of the TE0 mode at a 2.4 μm wavelength for an as-grown GeSn layer on a 2.5 μm thick Ge SRB on a Si substrate and for a GeSn layer on a SiN cladding. (b) Cross-sectional TEM images of GeSn on Ge SRB and a GeSnOI stack.

microdisk cavities was provided in Ref. [36]: the optical gain was strengthened with the GeSnOI technology thanks to the removal of the dense array of misfit dislocations array, the improved optical confinement and the improved heating dissipation. Another design with a thick AlN layer as a cladding could also be used to address optical confinement and thermal management issues [11].

As discussed in the next section, the transfer method using either AlN or SiN as dielectric claddings took advantage of the assets described above to reach for the first time RT lasing with GeSn. While both AlN and SiN are known to be transparent in the infrared, SiN should be used with caution. SiN layers deposited in a PECVD reactor with SiH_4 and NH_3 as precursors indeed contain a fairly large amount of hydrogen which has not desorbed. This results in the existence of N-H bonds producing high losses in the 2.8–3.5 μm wavelength range, as shown by transmission spectroscopy (Fig. 9a). No loss has been observed with PECVD-deposited SiN layers at wavelengths of 2.55 μm, however. The first continuous-wave lasing with GeSn was obtained at that wavelength with strained disks and PECVD-deposited SiN stressor layers. However, at wavelengths approaching 3 μm, N-H bonds are problematic. One could get rid of hydrogen in SiN layers with sputtering deposition methods instead of PECVD. The key advantage of using the SiN as cladding is strain engineering. It is indeed well known that, depending on the deposition process conditions used, the stress in SiN layers is adjustable across a broad spectrum, ranging from compressive to tensile (e.g. from −2 GPa to 2 GPa, typically). The use of − 1.7 GPa compressively stressed SiN enabled us to inject some tensile strain in the optically active GeSn layer. Thanks to patterning the GeSnOI layers into microdisk-shaped mesas, a portion of the strain was released and transferred to the GeSn layer (Fig. 9(b)), as shown by Finite Element Modelling (FEM). A relatively moderate tensile strain of around 0.6% could be injected by the SiN layer under the GeSn disk mesa (see Fig. 9(c), left). One can however increase the amount of injected tensile strain to 1.5–1.7% with an all-around geometry (see Fig. 9c right). Such a configuration is obtained after a selective underetching of the aluminum layer with respect to GeSn and SiN thanks to a KOH diluted solution. It results in a suspended GeSn microdisk. A conformal deposition of a second SiN layer over the whole structure then yields an all-around strained disk geometry with a homogeneous tensile strain in the disk periphery.

Fig. 9d shows Photo-Luminescence (PL) emission spectra for a GeSn layer with a Sn content of 14% in different configurations: blanket as-grown and transferred layers, after a patterning of the transferred layer into microdisk mesas and after an underteching of the Al layer followed by a second SiN stressor layer deposition to have an all-around stressor geometry. The transferred layer had a PL emission at the very same wavelength than that of the as-grown layer. This confirmed that the residual compressive strain of typically − 0.5% after epitaxy was still there after blanket layer transfer. A redshift of the PL peak after the etching of the transferred blanket layer into microdisk mesas was observed. The SiN stressor underneath injected some strain in the GeSn layer after patterning, as expected from FEM. The red shift was quite moderate, however (25 meV only), corresponding to an injected tensile strain of the order of 0.5% that is enough to have a dissipation of the residual compressive strain in the layer. The GeSn active region was then almost strain-free. The PL emission was redshifted by around 80 meV in the all-around geometry, corresponding to a final tensile strain state of 0.8–1%. Similar redshifts were observed when microdisk mesas and tensile strained disks were optically pumped in a pulsed regime above the lasing threshold (Fig. 9e).

3.2. Room temperature lasing in microdisk cavities

In the following, RT lasing from transferred GeSn layers is described in two configurations: (ultra-high tin content, zero strain), and (high tin content, high tensile strain). The first set of measurements were performed on a zero strain, ultra-high Sn content stack. The growth scheme employed to obtain the high quality, 17.2% of Sn lasing layer was different from the classical one where the layer of interest is directly grown onto the Ge buffer. Here, a step graded structure, with gradually increasing Sn concentration steps, was used to create a GeSn buffer on top of the Ge SRB. Most of the dislocations were confined in the lower Sn content steps, resulting in a high quality GeSn 17.2% Sn layer on top of such a step grading. This optically active layer was capped with lower Sn

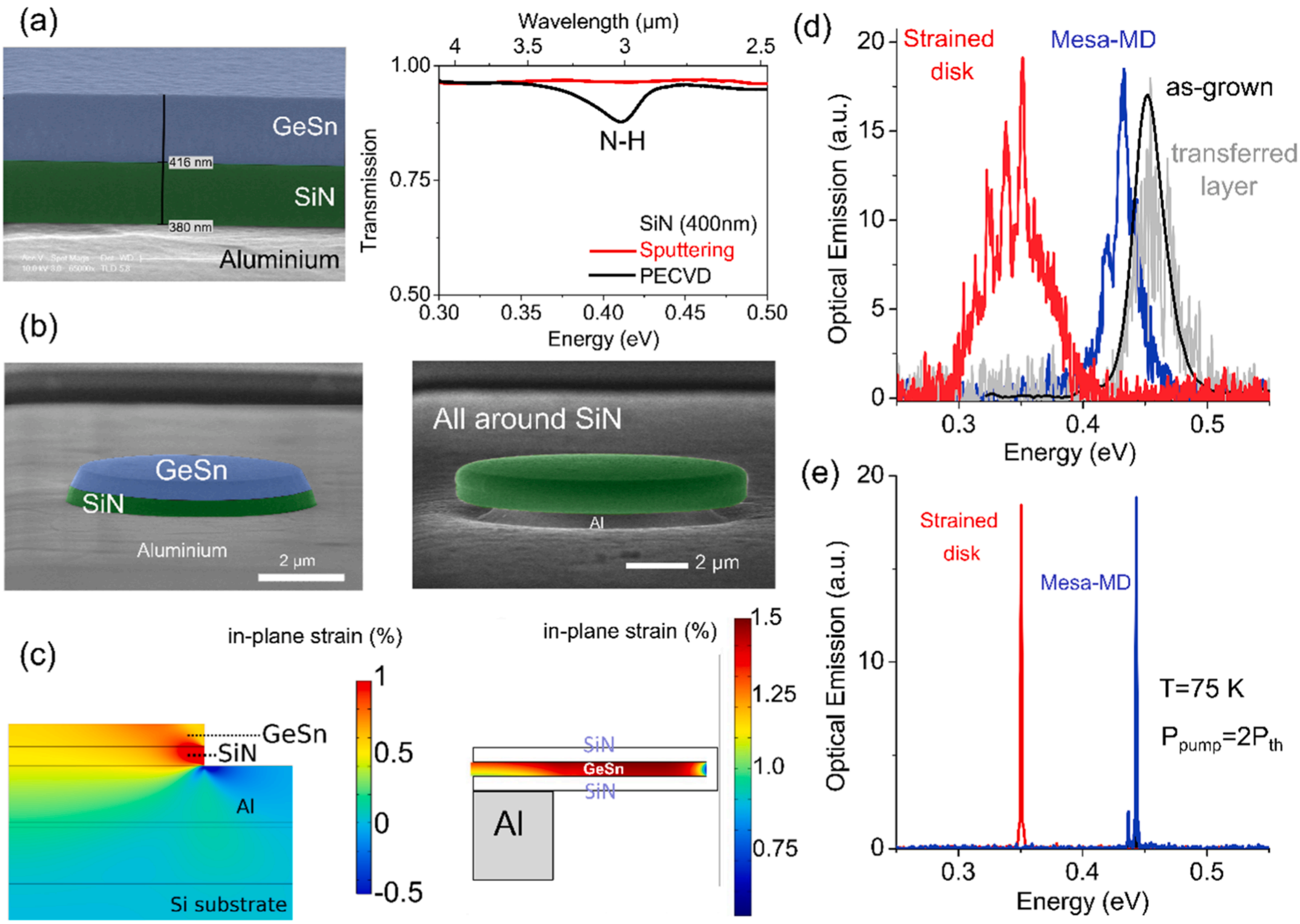

Fig. 9. (a) left: Scanning Electron Microscopy (SEM) picture of a GeSnOI stack with a SiN cladding, right: transmission spectra of 400 nm thick SiN layers deposited by PECVD and sputtering. (b) SEM picture of GeSnOI microdisk mesa (left) and suspended (right) microdisk with a second conformal deposition of SiN on the whole structure, with a complete wrapping of the GeSn disk by the stressor (All-around SiN stressor geometry) (c) FEM modelling of in-plane strain injected in a GeSnOI disk mesa (left) and a suspended microdisk with all-around geometry (right). (d) Photoluminescence spectra at 75 K of blanket as-grown and transferred layers as compared to PL spectra of microdisk-mesa and strained disk with an all-around stressor geometry. PL was measured under continuous wave optical pumping and the GeSn layer had a Sn content of 14%. (e) Measured emission from disk mesa and all-around strained disks under pulsed optical pumping above the lasing thresholds at 75 K.

concentration layers, grown at the very same temperature of 307 °C with lower $SnCl_4$ flows, to have some modest carrier confinement. The stack was then transferred on an AlN dielectric cladding [11]. The AlN choice was dictated both by its transparency in the Mid Infra-Red region, limiting absorption losses, and by its high thermal conductivity enabling efficient heat flux towards the substrate. Fig. 9a shows the AlN pedestal formation obtained by dipping in a resist developer containing Tetra-MethylAmmoniumHydroxide (TMAH) patterned micro-disks with different under-etching times. Fig. 9b shows a part of matrices containing different diameter disks, each one with the same underetch.

RT laser operation is obtained under pulsed pumping in this relaxed alloy (Fig. 10c), which has the highest Γ-L valley energy barrier reachable by increasing the Sn without the help of tensile strain. Fig. 10d presents spectra at 305 K obtained below and above the threshold. The energy barrier for relaxed 17% GeSn is indeed expected to be around 210 meV, as calculated in [37]. In Bjelajac et al., [38], the GeSn 14% layer was grown using a different strategy based on a single growth step process, without any additional confinement layers. In that case, the layer was bonded onto a SiN stressor, itself on aluminium, thinned down to remove the interfacial defects, and patterned into micro-disk mesas that were nearly fully relaxed due to the tensile strain transferred from the SiN to the GeSn as described in Fig. 10. RT lasing up to 300 K was reached with such micro-disks [38].

Should one uses lower tin contents, the energy barrier would decrease. As a consequence, the injection efficiency at the Γ point would degrade more rapidly as the temperature increases. In relaxed GeSn with 14% of tin, the barrier energy is expected to be around 154 meV [37]. The maximum lasing temperature was 265 K [39] with GeSn 14% layers grown in another reactor and the very same GeSnOI micro-disk mesa designs than in [38]. The use of SiN stressors in an all-around geometry enabled us to increase the Γ -L valley energy barrier in such GeSn 14% layers. A tensile strain of 0.8–1% was achieved in the resulting disk, with an increase of the barrier energy up to 190 meV, e.g. a value very similar to that in relaxed GeSn with 17% of Sn content. As a consequence, RT lasing was reached with 14% of Sn and tensile strain [39]. Fig. 11 shows the 3.5 μm wavelength lasing spectra at 300 K in such a strained GeSn disk with a tin content of 14%. Here the RT lasing threshold was in the hundreds of kW/cm^2 power density range.

The lasing thresholds as a function of temperature is plotted in Fig. 12 for (i) strain-free, suspended GeSn 17% on AlN pedestal micro-disks and (ii) GeSn 14%/SiN micro-disk mesas. The lasing thresholds of a tensile strained GeSn 14% micro-disk laser is also shown for comparison purposes. The tensile strain injected in GeSn layers with 14% of Sn enabled to reduce lasing thresholds by a factor of 2. As discussed in [32], the tensile strain lifted the valence band degeneracy, making the LH-band the highest energy band for holes. As a consequence, the global

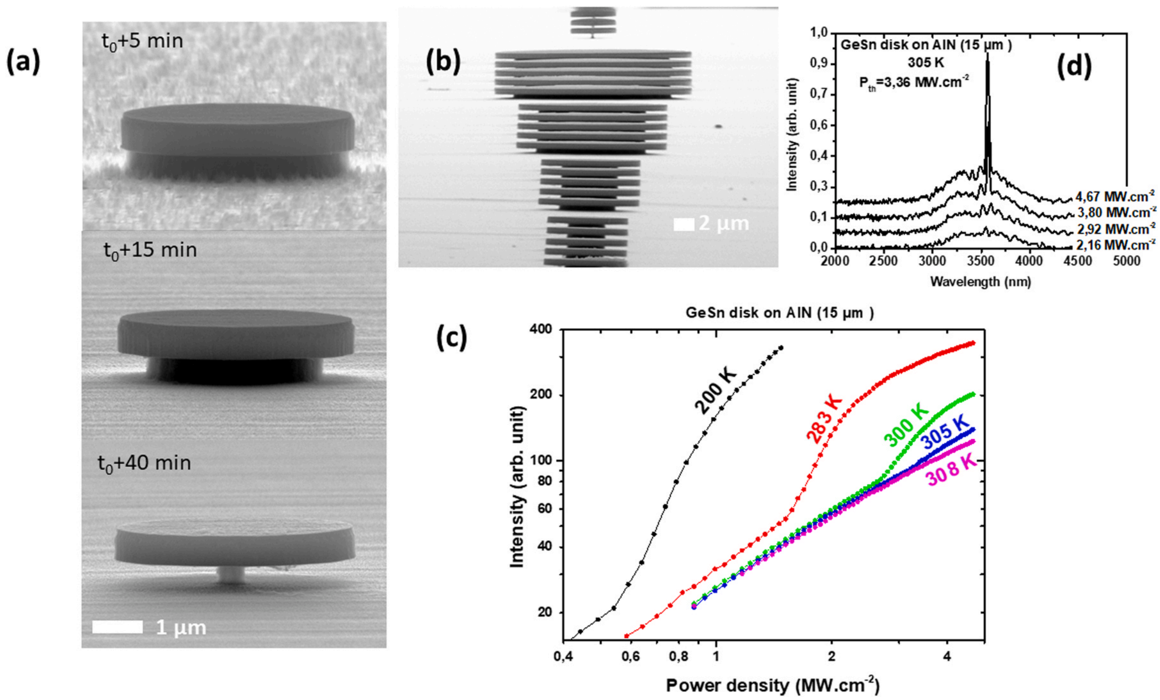

Fig. 10. (a) SEM pictures of micro-disks with different AlN pedestal diameters, (b) Arrays of GeSn microdisks with different diameters, (c) Light in-Light out curves on a 15 µm diameter disk under pulsed pumping at different temperatures and (d) below-above threshold spectra on a 15 µm disk on AlN obtained at 305 K under pulsed pumping.

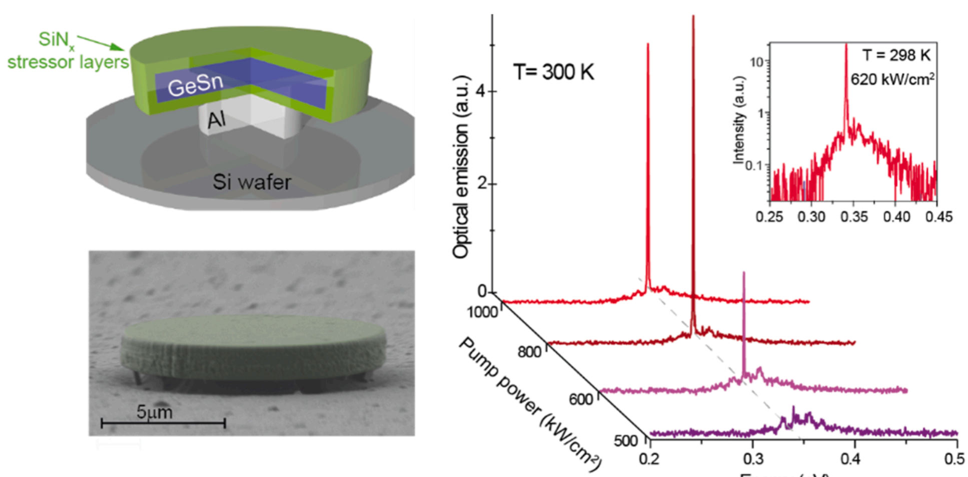

Fig. 11. Left: schematic and SEM view of a strained GeSn disk with a tin content of 14% and an all-around stressor geometry. Right: RT emission spectra from such 9 µm diameter disks as a function of the pulsed excitation. The inset shows a log plot of a spectrum above threshold at room temperature.

density of states was reduced as well as the excitation level needed to reach transparency and thus the lasing threshold. As discussed above, it also increased the Γ-L valley energy barrier, enabling us to reach RT lasing with 14% of Sn, as in strain relaxed GeSn with 17% of Sn. When comparing threshold variations in the 75 K-270 K temperature range, slopes were quite similar for suspended GeSn/AlN laser disks and suspended all-around tensily strained GeSn disks on SiN with 17% and 14% of Sn, respectively. However, the slope was drastically reduced for GeSn 17%/SiN microdisk mesas. This was likely explained by the fact that the mesa disk had an active region, at the disk periphery, that was not under-etched, enabling, upon optical pumping, an efficient heat dissipation in the substrate. For the strain relaxed 14% GeSn/SiN disk mesa, that should have similar cooling properties, the rapid threshold increase with the temperature could be explained by less efficient Γ-electron injection with increasing temperature due to a lower Γ-L energy barrier. Finally, for temperatures 270 K, slopes dramatically increased until the laser effect vanished close to RT. Currently, the origin of this common behaviour between strained and unstrained materials is not well understood and could be due to defect assisted or Γ to L thermally assisted electronic losses.

4. Optoelectronic GeSn components

4.1. Electrical contacts on GeSn-based materials

Engineering low-resistivity electrical contacts is an essential component in the quest for improving the efficiency of active photonic devices. The predominant metallization scheme reported for GeSn relies

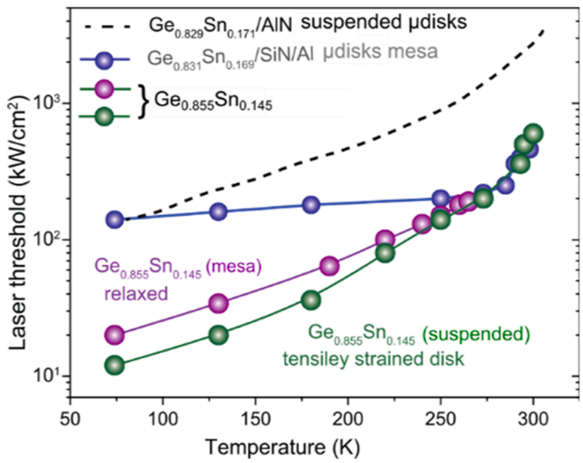

Fig. 12. Laser threshold dependence with temperature for transferred GeSn layers, in strain free micro-disk cavities suspended on AlN pedestals and micro-disk mesas with 17% or 14% of Sn, and for disks strained by SiN stressors in an all-around geometry on aluminum pedestals with a tin content of 14%.

on Ni contacts [40]. Ni(GeSn) exhibits low resistivity and contact resistance [41,42] at relatively low temperature [43]. A comprehensive study of the phase formation sequence during the solid-state reaction between Ni thin films and GeSn layers using various XRD analyses was performed. As illustrated in Fig. 13a, at low thermal budgets, the consumption of Ni and hexagonal Ni-rich ε-$Ni_5(GeSn)_3$ phase formation were evidenced. With a higher thermal budget, the consumption of the Ni-rich phase and the formation of the orthorhombic mono-stanogermanide phase Ni(GeSn) were highlighted [44]. On the other hand, the primary drawback of the Ni/GeSn system is its limited thermal stability, attributed to two specific phenomena: Ni(GeSn) agglomeration and Sn segregation [45]. As shown in Fig. 13b, at 350 °C, Sn begins to preferentially segregate at grain boundaries and on the surface. At 400 °C and beyond, the Ni(GeSn) layer agglomerates and Sn segregation persists [46].

Various technological alternatives have been assessed to boost the thermal stability of the Ni/GeSn system. Taking into account the complete metallization module, one can play on various technological levers, from GeSn surface engineering to annealing and metallization schemes. GeSn layers surface preparation by wet and plasma treatments prior to metallization and its impact on solid-state reactions was first investigated [47]. The impact of alloying Ni with Pt or Co was also quantified. These alloying elements positively impact Sn segregation by delaying it (e.g. postponing it to higher temperatures). The addition of Co had a minimal impact on both the morphological and electrical properties. However, Pt enhanced the surface morphology by delaying the agglomeration of the Ni(GeSn) phase, expanding the operational window wherein the sheet resistance remained at lower level [48,49].

The use of pre-amorphization by implantation (PAI) was also assessed before metallization [50,51]. C implantation had a positive impact on surface morphology by retarding Sn long-range diffusion and Ni(GeSn) agglomeration [51]. Alternative metallization schemes using for instance Ti were also evaluated [52,53].

Ni-GeSn alloys were produced in most cases through rapid thermal annealing (RTA). Alternative annealing processes could also be used to enhance the Ni / GeSn system thermal stability. Recently, laser thermal annealing (LTA) [54,55] was examined to restrict the thermal exposure that stacks underwent. LTA showcased its capacity to create low-resistance Ni-based contacts on GeSn, with an enhanced thermal stability [55].

4.2. GeSn light emitting devices

Several bulk GeSn Light Emitting Diodes (LEDs) with low Sn contents were reported with light emission in the range 1.8 and 2.5 µm [56–60]. $Ge_{0.91}Sn_{0.09}$ LED exhibit a emission power of 58 nW at 2.57 µm under an injection current of 100 mA [60]. These LEDs did not exhibit any direct bandgap behaviour. Higher emission wavelengths up to 3.4 µm were achieved with GeSn bulk LEDs for Sn contents up to 16% [61,62]. Such LEDs were used to detect methane in gas sensor cells [63]. Fig. 14(a) shows the emission spectra of a $Ge_{0.85}Sn_{0.15}$ LED at RT for different currents. Carrier confinement appeared to be unsatisfactory at room temperature for efficient light emission. To overcome this limitation, multiple GeSn/Ge quantum wells were evaluated [64]. Compared to n-type Ge LEDs, a fivefold increase in electroluminescence emission was achieved [65]. However at room temperature, it appeared that Ge barriers still inadequately confined GeSn carriers.

SiGeSn alloys were introduced to achieve type-I band alignment with GeSn alloys. Efficient light emission was demonstrated in an almost strain-free stack with 10.9% of Sn and 10.5% of Si in the SiGeSn barrier layers [66]. Emission spectra of a GeSn/SiGeSn MQW and of a homojunction LED at 4 K and 300 K are showed in Fig. 14b.

Increasing the Si/Sn ratio increases the SiGeSn barrier height. However, determining the precise band alignment between SiGeSn and

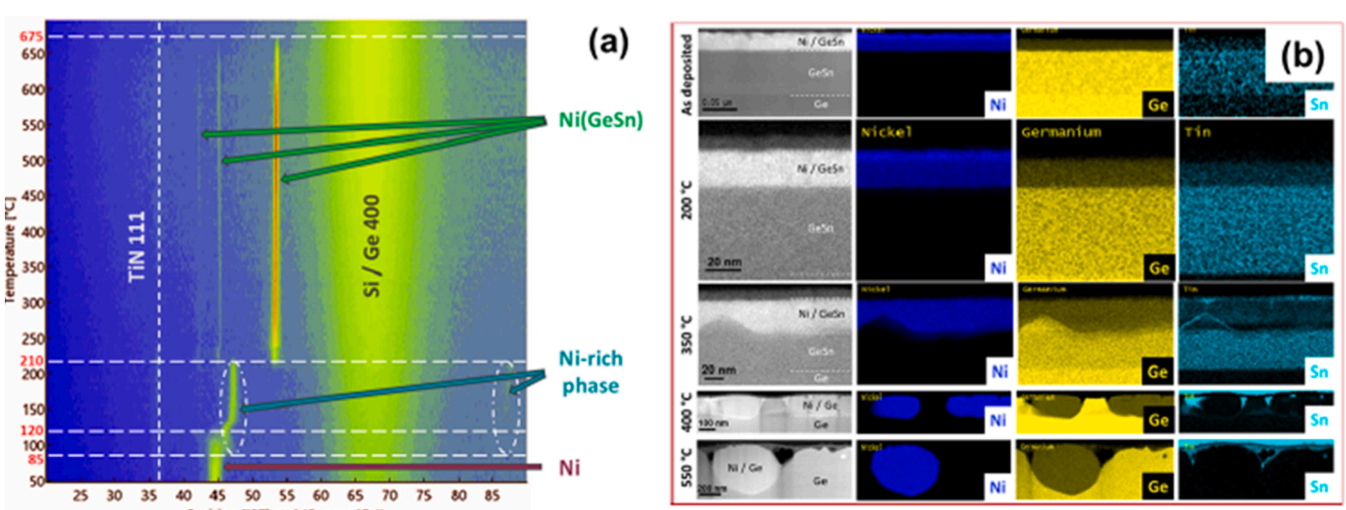

Fig. 13. (a) In-situ XRD analysis of the solid-state reactions between 10 nm of Ni and $Ge_{0.9}Sn_{0.1}$ [48] and (b) Cross-sectional TEM images coupled with EDX analyses of $Ge_{0.9}Sn_{0.1}$ samples in their as-deposited state and after RTA annealing during 30 s at 200, 350, 400 and 550 °C in N_2 [51].

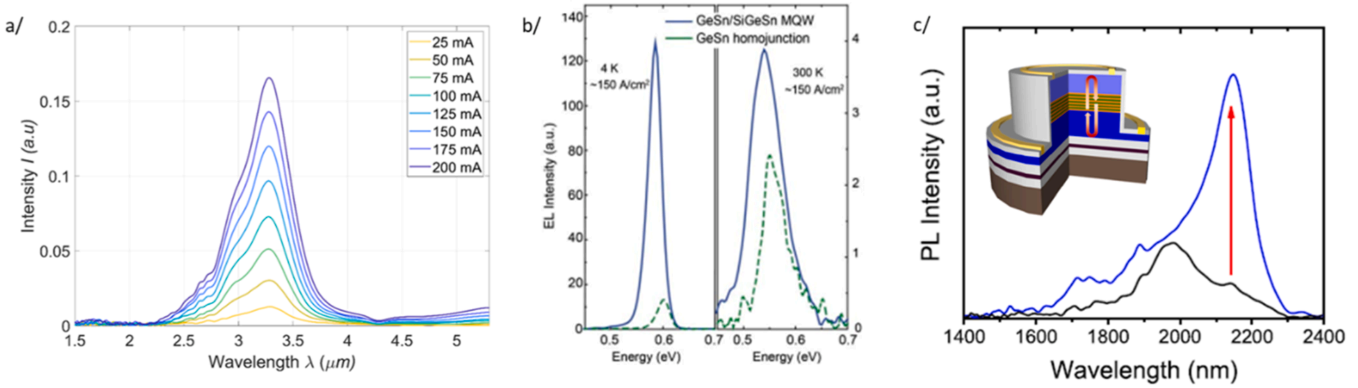

Fig. 14. a/ $Ge_{0.85}Sn_{0.15}$ LED emission spectra for different currents. b/ Emission spectra at 4 K and 300 K of homojunction (dashed green) and GeSn/SiGeSn MQW (blue) LEDs. c/ RT photoluminescence spectra of a GeSn MQW vertical-cavity-surface emitting structure and of GeSn MQWs grown on Si substrates. Inset: Schematic of the vertical-cavity-surface emitting LEDs.
(a) Reproduced with permission from [62]. (b) Reproduced from [66]. (c) Reproduced from [70].

GeSn poses a challenge. Multiple SiGeSn/GeSn quantum well LEDs was evaluated, with 5% of Sn and 10% of Si in the SiGeSn layers [67]. A higher super-linear electroluminescence were achieved compared to conventional GeSn/Ge heterojunction LEDs. This implies that radiative recombination was effective in these devices. [68].

Vertical-cavity-surface emitting light sources offer several advantages for out-of-plane light coupling, high bandwidth and spectral emission control. $Ge_{0.92}Sn_{0.08}$/Ge MQW LEDs grown on 300 mm wafers showed operation at 2 µm wavelength [69]. The 300 mm wafer was bonded wafer level to a 200 mm wafer [70]. At the resonant wavelength, an emission enhancement factor of 8 was achieved compared to the reference MQW structure. Table 1 summarizes key parameters of GeSn LEDs at RT previously discussed.

4.3. SiGeSn electrically injected lasers

Monolithic integration could be facilitated by SiGeSn-based band-to-band lasers grown on Si substrates using all-group-IV direct-bandgap materials [29,71–74]. Research on laser devices moved in recent years from optical pumping to electrical injection [75,76]. Reaching lasing through electrical injection presents more challenges compared to lasing under optical pumping, however [75]. For instance, doping leads to increased free carrier absorption losses. The use of metal contacts also results in additional optical loss. The appropriate metal should be selected to fabricate good ohmic contacts and so on. Such challenges need to be overcome to obtain electrically pumped lasing [76].

The first electrically injected SiGeSn laser was reported in 2020 [6]. A schematic representation in cross-section of the laser device is shown in Fig. 15(a). In-situ doping was used to obtain the n-type and p-type layers. P-type and n-type electrodes were coated with chromium (Cr) and gold (Au) using electron beam evaporation with 10 and 350 nm thicknesses, respectively. The Si substrate was thinned down to 140 µm. Subsequently, facet cleaving was performed to create the Fabry-Perot cavity.

The electronic band diagram is shown in Fig. 15(b). Four sub-bands were taken into account, including indirect L (EcL) and direct Γ (EcΓ) valleys in the conduction band (CB), as well as heavy hole (Evhh) and light hole (Evlh) sub-bands in the valence band (VB). The following features were obtained: i) the $Ge_{0.89}Sn_{0.11}$ active layer presents a direct bandgap with an energy difference of 84 meV between Γ and L valleys. As the light emitting layer is almost fully relaxed, there is an overlap at the top of light hole (LH) and heavy hole (HH) bands; ii) both L and Γ valleys in the CB present type-I band alignments due to the larger bandgap energies of the $Si_{0.03}Ge_{0.89}Sn_{0.08}$ cap and of the GeSn buffer with lower Sn contents. The graded Sn concentration in the GeSn buffer (from 8% up to 11% in the growth direction) resulted in an energy decrease of L and Γ valleys (the L valley slower than the Γ one); iii) the HH band presents in the VB a type-I band alignment. However, the LH band exhibits a type-II band alignment at the interface between the cap and the active layer. This is attributed to the tensile strain present in the $Si_{0.03}Ge_{0.89}Sn_{0.08}$ cap. This results in a hole leakage channel, with therefore a lasing threshold increase. To address that issue, the top SiGeSn layer was intentionally p-type doped. Holes coming from the SiGeSn cap layer flew towards the GeSn active region and saw a hole barrier at the interface between the GeSn active region and the GeSn buffer. As a result, holes were effectively confined in the active region, facilitating population inversion.

Typical pulsed light-current (LI) curves from the device with a cavity length of 0.8 mm are depicted in the plot of Fig. 16(a) at temperatures up to 100 K, the maximum lasing temperature. The threshold current

Table 1
Characteristics of GeSn-based LED at room temperature. (RPCVD: Reduced Pressure - Chemical Vapor Deposition, MBE: Molecular Beam Epitaxy).

Epitaxy	Types of stacks	GeSn composition (%)	Biaxial strain	Emission Wavelength (µm)	Ref.
MBE	Ge/GeSn/Ge heterostructures	4.5	- 0.66%	1.9	[59]
	Ge/GeSn/Ge heterostructures	7.8	———	2.2	[56]
	Ge/GeSn/Ge heterostructures	9.7	———	2.25	[58]
	SiGeSn/GeSn/SiGeSn MQW	8.5	- 1.6%	2.06	[11]
CVD	Ge/GeSn/Ge heterostructures	9.2	- 0.48%	2.2	[57]
	Ge/GeSn/Ge heterostructures	9	-0.24%	2.5	[60]
	Ge/GeSn/Ge heterostructures	8	———	2.06	[68]
	Ge/GeSn/Ge heterostructures	13	- 0.5%	2.8	[63]
	Ge/GeSn/Ge heterostructures	16	- 0.66%	3.4	[61]
	SiGeSn/GeSn/SiGeSn MQW	9.1	- 0.1%	2.2	[66]
	Ge/GeSn/SiGe MQW	8	- 1.16%	2.14	[70]

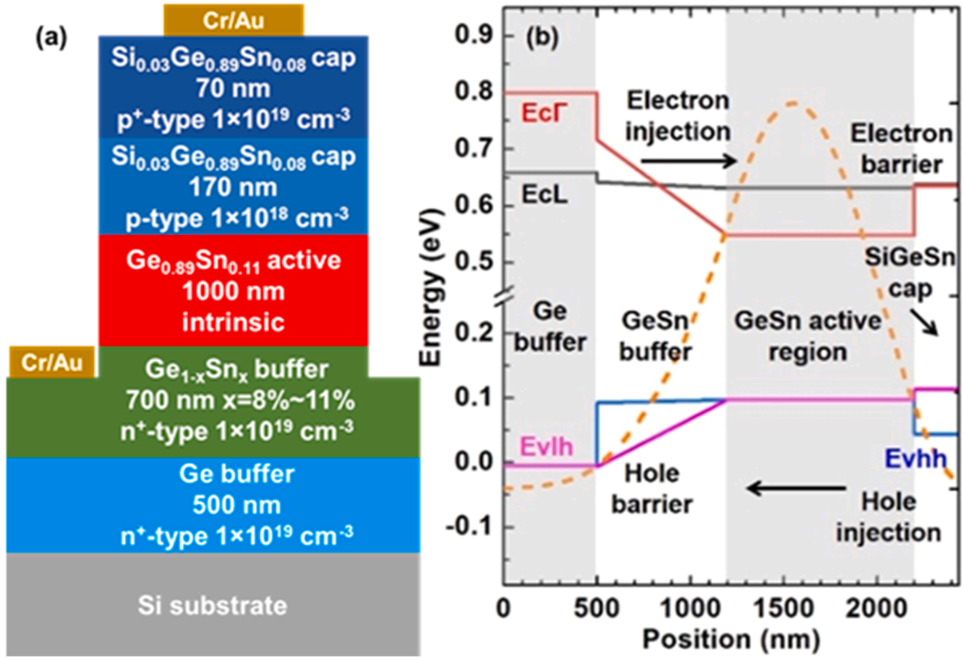

Fig. 15. (a) Schematic representation in cross-section of an electrically pumped laser device; (b) Band structure computations and profile of the fundamental TE mode. There is a type II band alignment between SiGeSn cap layers and GeSn active layer at the LH band. The GeSn active region exhibited an optical field overlap of 75%.
Reproduced from [21].

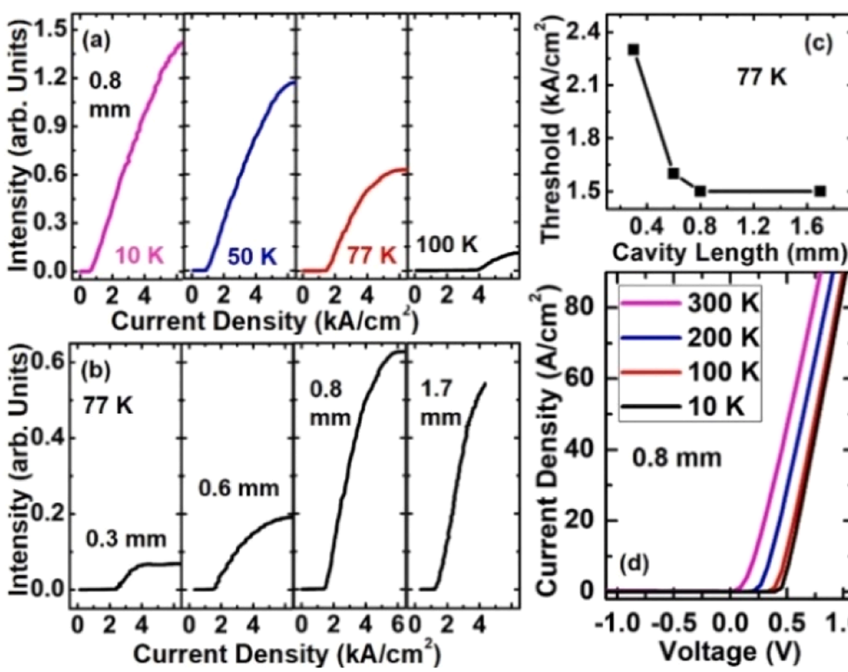

Fig. 16. (a) LI curves from 10 to 100 K of a 0.8 mm cavity length device; (b) LI curves for four devices with varying cavity lengths at 77 K; (c) Threshold at 77 K of each device; (d) Temperature-dependent IV characteristics of the 0.8 mm cavity length device.
Reproduced from [21].

densities are 0.74 kA/cm^2 at 10 K and 3.9 kA/cm^2 at 100 K, respectively. At 10 K, the emission saturates at 7.5 kA/cm^2. The LI characteristics of devices with cavity lengths of 0.3, 0.6, 0.8, and 1.7 mm are shown in Fig. 16(b) at 77 K. Threshold current densities were plotted at 2.3, 1.6, 1.5, and 1.5 kA/cm^2, respectively (Fig. 16(c)). As the cavity length (L) increased from 0.3 up to 0.6 mm, the lasing threshold experienced a significant reduction. This reduction was primarily attributed to decreased mirror losses. ($\propto 1/L$). When the cavity length was longer than 0.6 mm, other loss mechanisms became dominant. Very little threshold changes were obtained, then. The typical IV characteristics of the 0.8-mm cavity length device are shown in Fig. 16(d). The series resistance was found to be 2.85 Ω. The turn-on voltage of the device varied within the range of 0.03 to 0.12 V from 300 to 10 K. The small turn-on voltage was due to the narrow bandgap of GeSn.

Following the first demonstrated electrically injected laser, many efforts were made to improve laser performances thanks to various device structures. Five samples were grown to investigate the impact of the cap layer thickness, the cap layer material and the Sn composition in the active region. Data are provided in Table 2 and the three sets of experiments shown in Fig. 17. Samples A and C had thicker caps than samples B and D. $Si_{0.03}Ge_{0.89}Sn_{0.08}$ with a 114 meV barrier height was used in the caps of samples A and B, compared to $Ge_{0.95}Sn_{0.05}$ with a 58 meV barrier height in the caps of samples C and D. Samples A and E had Sn compositions of 11% and 13% in the GeSn active layers, respectively.

The use of thicker caps resulted, regardless of the cap material, in lower lasing thresholds and an increased maximum operating temperatures, as presented in Fig. 18 (samples A versus B and C versus D). Indeed, thicker cap layers reduced optical losses from the metal contact and increased the optical confinement factor in the active region. However, free carrier absorption losses also increased due to the presence of heavily doped caps. Performances were also higher for samples with $Si_{0.03}Ge_{0.89}Sn_{0.08}$ instead of $Ge_{0.95}Sn_{0.05}$ caps (samples A versus C and B versus D). The higher barrier height reduced the lasing threshold and increased the maximum lasing temperature thanks to improved electron confinement.

Earlier investigations into optically pumped lasers showed that a Sn concentration increase in the active region led to a rise in the maximum operating temperature and a decrease in the lasing threshold [76]. However, the device with a higher Sn content in the active region showed an increased lasing threshold and a reduced maximum operating temperature. This can be interpreted as follows: optically pumped lasers depend on optical absorption to collect carriers. the absorption coefficient rises at a particular incident light wavelength, as the Sn concentration increases because of a narrower bandgap. Nevertheless, the carrier injection efficiency does not exhibit significant improvement with sample E. As an active region with a higher Sn concentration results in a larger tensile strain in the cap layer, the increased hole leakage due to type-II band alignment for the LH band would reduce the carrier injection efficiency. A SiGeSn cap with the appropriate Sn and Si compositions in order to reduce the tensile strain while maintaining a large enough barrier height would be more suitable. Characteristics for different laser devices are outlined in Table 3.

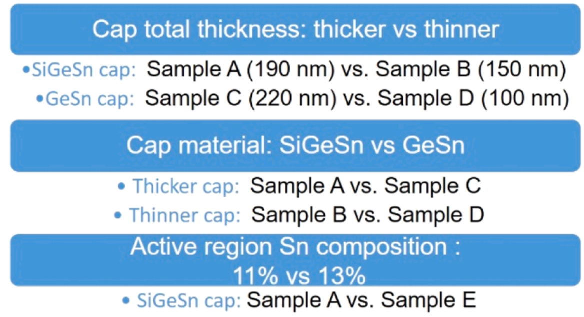

Fig. 17. Three sets of experiment to quantify the impact on lasing of the cap thickness, the cap material and the active region Sn composition. Reproduced from [30].

4.4. Progress in GeSn light detecting devices

GeSn alloys can extend light detection to definitely longer wavelengths in the mid-infrared. The development of GeSn-based photodetectors is briefly described in this following section. Table 4 and Table 5 present key performances of selected GeSn photoconductive detectors and GeSn pin detectors. We show that the performance of photodetectors is increasing over the years.

4.4.1. GeSn photoconductive detectors

Several bulk GeSn photoconductors were first reported at wavelengths ranging from 1.9 µm to 2.4 µm, with GeSn thicknesses varying from a few tens of nm to a few hundreds of nm [77,78]. The evolution of the specific detectivity of a $Ge_{0.9}Sn_{0.1}$ photoconductor as a function of temperature is presented in Fig. 19a. A significant increase of the detectivity was obtained at 77 K compared to that at room temperature. Photodetectors with three Ge/GeSn quantum wells with 9% of Sn in the wells showed a sensitivity of 0.1 A/W at 5 V [79].

Higher Sn contents photoconductors were later on reported, with cut-off wavelengths up to 4 µm at RT [80]. Specific detectivities at RT are currently below that of PbSe detectors. The dark current of photoconductors has been greatly improved using GeSn membranes with a Sn content of 17% [81]. Fig. 20 shows the contacted photoconductive GeSn membrane and its associated dark current and responsivity compared to that of an as-grown $Ge_{0.83}Sn_{0.17}$ photoconductor. The mid wavelength infrared (MWIR) was reached by releasing the residual compressive strain in the thick GeSn layer, with a cut-off wavelength above 4.5 µm (Fig. 20c).

4.4.2. GeSn pin detectors

The most commonly used detector for Si-based optoelectronic applications is the pin detector, which typically consists in doped layers sandwiching a non-intentionally doped absorbing layer. The first CVD grown GeSn photodetectors contained 2% of Sn [82]. A wavelength cut-off of 1750 nm was then achieved, covering the entire telecommunications wavelength. GeSn photodetectors with 700 nm thick stacks, n-doped and p-doped Ge carrier collection layers and at most 11% of Sn in the GeSn absorbing layer were evaluated in [74] (Fig. 21a). An external quantum efficiency of 20% and a peak responsivity of 0.32 A/W at 2 µm were measured at RT with a cut-off wavelength of 2.65 µm. Fig. 21b shows the specific detectivity (D*) of these $Ge_{0.89}Sn_{0.11}$ photodetectors at 77 K and room temperature. At 2 µm, its detectivity is ten times lower than that of an extended InGaAs detector. It should be noted that all D* reported here were obtained using the calculated noise extracted from I(V) curves.

Dual-band vertical detectors were fabricated on $Ge_{0.905}Sn_{0.095}$/Ge/Si stacks, the aim being the switching of the spectral response of the resulting devices between two distinct infrared bands. Such a feature is an important step towards multispectral imaging [83]. The double junction n-i-p-i-n structures showed specific detectivities above 1.9×10^{10} cm.Hz$^{1/2}$. W^{-1} up to 1.6 µm with the Ge strain relaxed buffer as the absorption layer and 4.0×10^{9} cm.Hz$^{1/2}$. W^{-1} with GeSn as the absorption layer (Fig. 22a). Broadband operation in the SWIR region

Table 2
laser structure summary (Reproduced from [30]).

Sample	p-type Cap			GeSn Active Region			n-type Buffer	
	Material	Thickness (nm)	ΔE_c* (meV)	Sn %	Thickness (nm)	Lasing wavelength at 10 K (nm)	Material	Thickness (nm)
A	$Si_{0.03}Ge_{0.89}Sn_{0.08}$	190	114	11.2	610	2238	$Ge_{0.93}Sn_{0.07}$	950
B	$Si_{0.03}Ge_{0.89}Sn_{0.08}$	150	114	10.8	430	2281	$Ge_{0.93}Sn_{0.07}$	670
C	$Ge_{0.95}Sn_{0.05}$	220	58	11.2	520	2294	$Ge_{0.93}Sn_{0.07}$	650
D	$Ge_{0.95}Sn_{0.05}$	100	58	11.5	450	2272	$Ge_{0.93}Sn_{0.07}$	610
E	$Si_{0.03}Ge_{0.89}Sn_{0.08}$	180	131	13.1	540	2654	$Ge_{0.93}Sn_{0.07}$	540

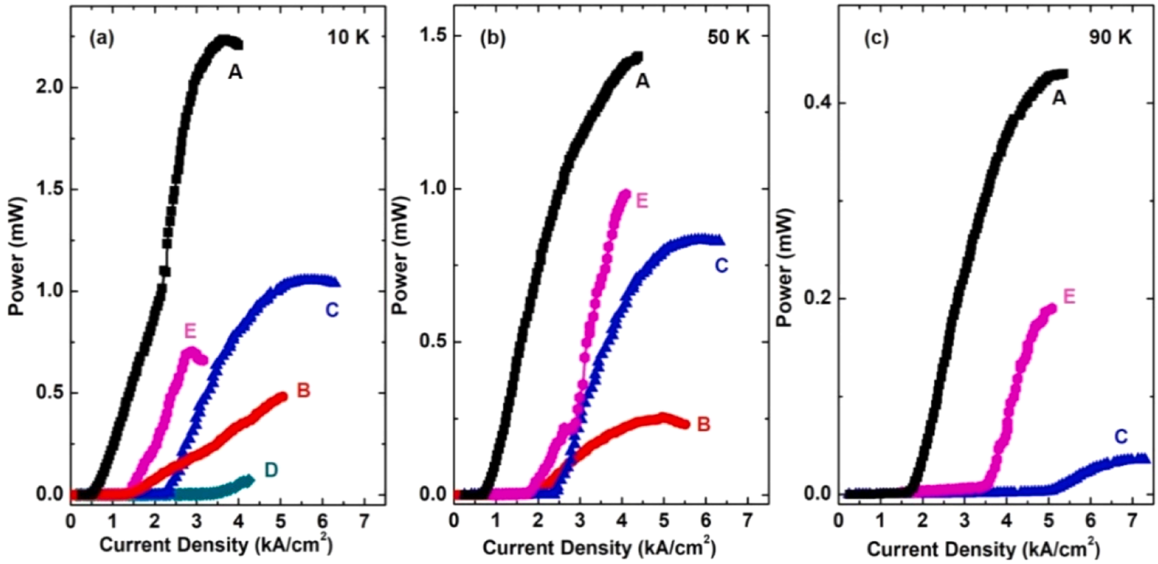

Fig. 18. L-I curves of each sample at (a) 10 K; (b) 50 K; and (c) 90 K.
Reproduced from [30].

Table 3
Summary of laser characteristics (Reproduced from [30]).

Sample	Cap Layer Material	Cap Layer Thickness (nm)	Sn % in Active Region	Threshold at 10 K (kA/cm^2)	Threshold at 77 K (kA/cm^2)	T_{max} (K)	Lasing Wavelength at 10 K (nm)
A	$Si_{0.03}Ge_{0.89}Sn_{0.08}$	190	11	0.6	1.4	100	2238
B	$Si_{0.03}Ge_{0.89}Sn_{0.08}$	150	11	1.4	N.A.	50	2281
C	$Ge_{0.95}Sn_{0.05}$	220	11	2.4	3.1	90	2294
D	$Ge_{0.95}Sn_{0.05}$	100	11	3.4	N.A.	10	2272
E	$Si_{0.03}Ge_{0.89}Sn_{0.08}$	180	13	1.4	2.9	90	2654

Table 4
Key figures-of-merit of GeSn-based photoconductive detectors: responsivity at different wavelengths and associated dark current.

Year	Sn (%)	Structure	Responsivity (A/W) at room temperature	Peak D* (cm·Hz$^{1/2}$·W^{-1})	Cut-off wavelength (μm)	Reference
2012	9	GeSn/Ge QW	1 at 5 V - 1.55 μm 0.1 at 5 V - 2.2 μm	——	2.2	[79]
2014	7	Bulk - 240 nm	0.265 at 10 V - 1.55 μm (at 77 K)	5×10^9	2.4	[77]
2015	10	Bulk – 95 nm	0.26 at 8 V – 1.55 μm	4×10^9	2.4	[78]
2018	8	Bulk – 100 nm	0.1 at 2 μm	——	2	[79]
2019	12.5	Bulk – 660 nm	2	1.1×10^{10}	2.95	[80]
	15.9	Bulk – 670 nm	4.4×10^{-2}	5.5×10^8	3.2	
	17.9	Bulk – 254 nm	3.8×10^{-3}	4.4×10^8	3.35	
	20	Bulk – 950 nm	6.74×10^{-3}	1.1×10^8	3.65	
	22.3	Bulk – 850 nm	3.2×10^{-3}	1.1×10^8	3.65	
2021	17	Bulk – 160 nm	1×10^{-2}	——	3.5	[81]
	17	Relaxed Bulk – 160 nm	3.3×10^{-3}	——	4.6	

Table 5
Sn content, devices structures, wavelength cut-off and responsivity of GeSn pin photodetectors.

Year	Sn (%)	Structure	Responsivity (A/W) at room temperature	Peak D* (cm·Hz$^{1/2}$·W^{-1})	Cut-off wavelength (μm)	Reference
2009	2	Bulk – 350 nm	0.05 at − 0.16 V	——	1.75	[82]
2018	11	Bulk – 300 nm	0.32 at 2 μm	1.7×10^9	2.65	[83]
2020	8	GeSn/Ge MQW	0.31 at 1.55 μm	1.37×10^{10}	2.2	[85]
2020	8	GeSn/Ge MQW	0.11 at 2 μm	2.14×10^8	2.26	[87]
2021	9.5	Bulk – 700 nm	0.64 at 1.9 μm	4×10^9	2.6	[83]
2021	8	GeSn/Ge MQW	0.0085 at 2 μm	1×10^9	2	[86]
2021	4.9	Bulk – 350 nm	0.0014 at 2 μm	——	2	[15]
2022	10	Bulk – 300 nm	0.3 at 1.55 μm	3.8×10^8	2.6	[84]
2023	8	GeSn/Ge MQW	0.232 at 1.55 μm	5.34×10^9	2	[88]
2023	15	Bulk – 480 nm	0.2 at 1.55 μm	1×10^8	3.5	[90]

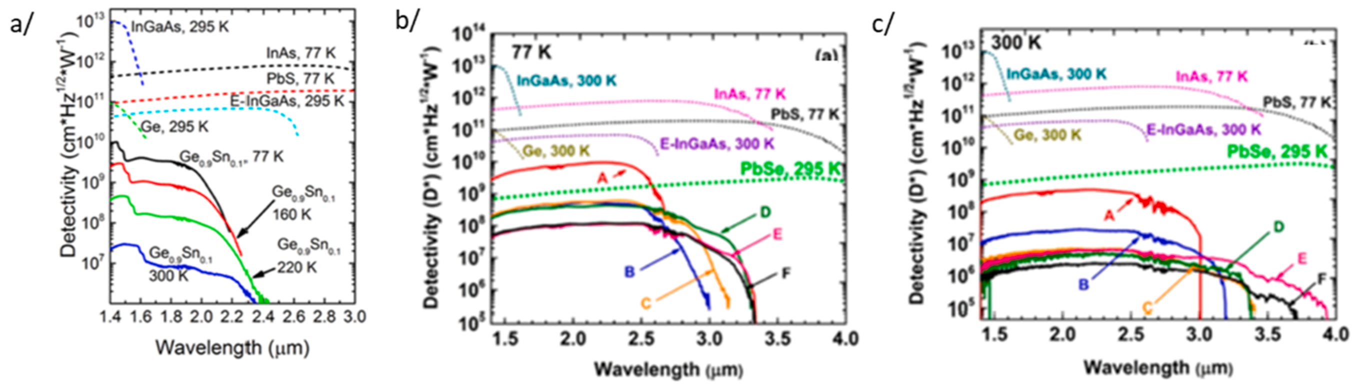

Fig. 19. Specific detectivities versus temperature of (a) a $Ge_{0.9}Sn_{0.1}$ photoconductor; reproduced from [74], OSA Publishing, open access, 2014, and of various Sn content GeSn photoconductive detectors. Sn contents for samples A–F were 12.5%, 15.9%, 15.7%, 17.9, 20.0%, and 22.3%, respectively, (b) at 77k and (c) at 300 K. Reproduced from [77].

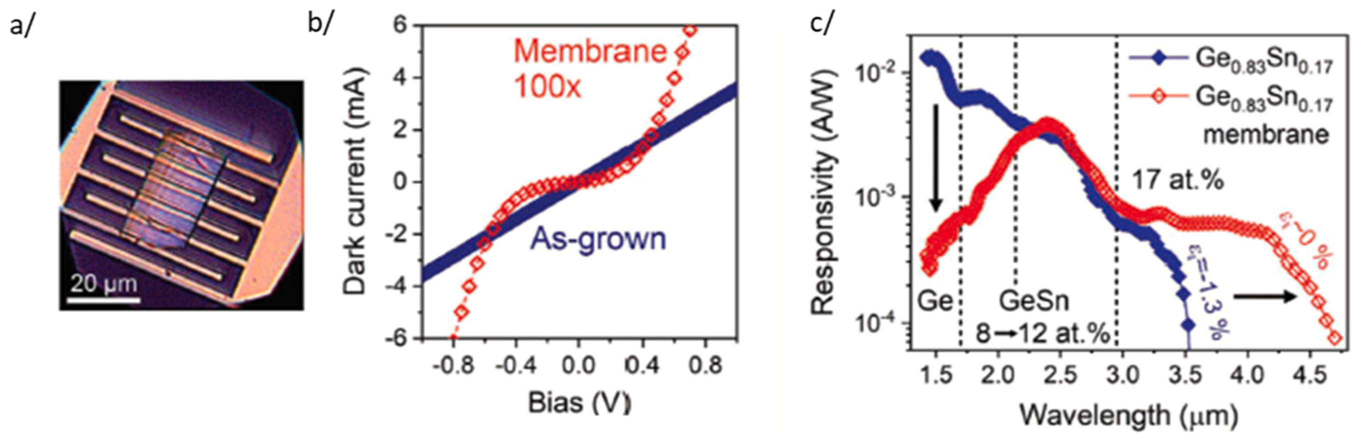

Fig. 20. (a) Optical image of suspended membranes photoconductors, (b) dark current and c/ responsivity of membrane and as-grown $Ge_{0.83}Sn_{0.17}$ photoconductors. Reproduced from [81].

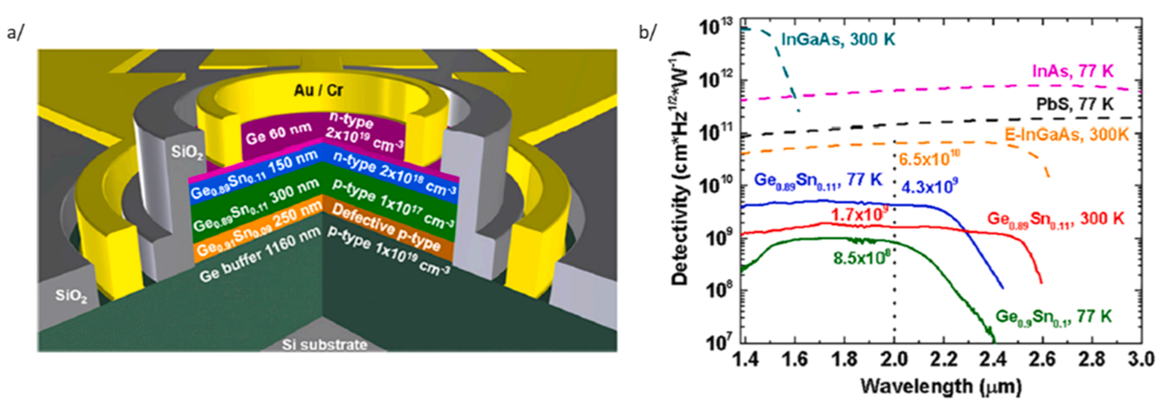

Fig. 21. a/ Schematic of a $Ge_{0.89}Sn_{0.11}$ photodiode with a RPCVD-grown stack, b/ Specific detectivity of photodiodes at 77 K and 300 K with a bias of − 0.1 V. Reproduced from [81].

was also obtained in GeSn photo-detectors. A peak sensitivity of 0.3 A/W was achieved with $Ge_{0.909}Sn_{0.091}$ at room temperature, with a bandwidth reaching 7.5 GHz at 5 V bias (Fig. 22b) [84]. Such GeSn detectors with a cut-off wavelength of 2.6 μm and $D^* = 3.8 \times 10^8$ cm. $Hz^{1/2}$. W^{-1} were used to diagnose ultrashort pulses from a super-continuum laser with a temporal resolution in the picosecond range. It is important to highlight that despite GeSn photodetectors being at the early stages of development, they can already offer high-speed operation at 2.5 μm that is out of reach in conventional III-V and II-VI technologies. More research and development is however required to significantly decrease the dark current and improve D*. To this end, structural defects are now the major source of leakage in GeSn devices.

GeSn exhibits a substantial lattice mismatch with Si and Ge, resulting in numerous misfit dislocations above the critical GeSn thickness for plastic relaxation (typically, a few tens of nm) and steeply increasing the strong dark current in GeSn photodetectors. The use of GeSn wells sandwiched by Ge or SiGeSn barriers with a lattice parameter similar or equal to that of Ge SRBs is attractive to circumvent plastic relaxation and

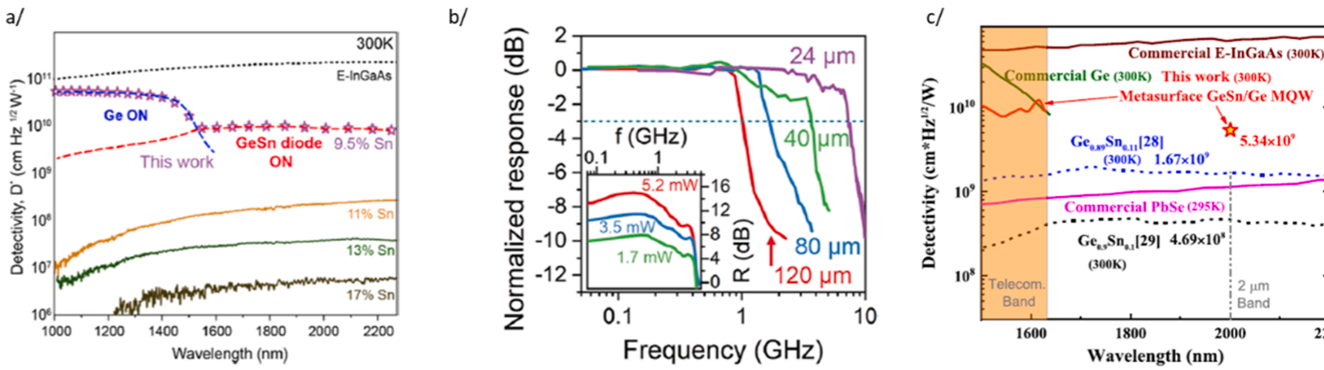

Fig. 22. (a) Wavelength-dependent specific detectivity for a Ge/GeSn dual-band detector. Reproduced from [80], ACS publication, 2021, (b) Normalized photo-response of different diameter $Ge_{0.909}Sn_{0.091}$ photodetectors at - 5 V reverse bias showing the bandwidth response of the optical pulse frequency. Reproduced from [81]. (c) Specific detectivities of surface structured GeSn/Ge MQW photodetectors at 2 µm. Reproduced from [84].

gain access to thicker absorbing layers with reduced dark currents. Attempts to improve the performance of GeSn photodetectors using MQWs were made [85,86]. Surface structuring of the GeSn MQW increased the responsivity by an order of magnitude, reaching 0.232 A/W at 2 µm, and slightly increased the dark current density, reaching a D* of 5.34 × 10^9 cm.$Hz^{1/2}$. W^{-1} [87,88]. This specific detectivity is higher than that of commercial InSb and PbSe photodetectors at 2 µm (Fig. 22c).

Other approaches were investigated to improve the performances of GeSn photodetectors, such as the growth of GeSn photodetectors on SOI substrates [89]. $Ge_{0.85}Sn_{0.15}$-based photodetectors showed detectivities above 10^8 cm.$Hz^{1/2}$. W^{-1} at 1.55 µm and a cut-off wavelength of 3.5 µm, enabling the tracking of light absorption by methane [90].

The main performance metrics of pin GeSn detectors are summarized in Table 5.

5. Outlook and conclusion

Fabricating an entire mid-IR photonic circuit in a standard CMOS foundry, solely from group-IV semiconductors, would be highly desirable. GeSn-based materials would provide efficient light emitters, photodiodes and modulators, all relying on direct bandgap emission and absorption. Encouragingly for silicon photonics, GeSn films and devices have successfully been fabricated using industry-standard CMOS epitaxy tools and conventional clean room techniques. These developments strongly support the inclusion of GeSn alloys in material roadmaps. However, several challenges remain: (i) Lattice mismatch: GeSn has a significant lattice mismatch with the Ge strain relaxed buffers typically used as templates on silicon substrates. During growth, this mismatch results in the formation of numerous interfacial defects that should ideally be eliminated or at least minimized, (ii) Low temperature growth defects: out-of-thermodynamic-equilibrium, low-temperature growth processes often result in a high number of bulk point defects. These defects typically lead to strong residual p-type doping and have a negative impact on carrier mobility, necessitating defect mitigation strategies, (iii) Unresolved issues: numerous open questions remain, including the band alignment at Ge/(Si)GeSn interfaces and the development of predictive band structure simulations.

Despite these challenges and a still incomplete knowledge of material parameters, a combination of two approaches - external strain and Sn alloying - led to remarkable GeSn laser technology improvements. These achievements include low-threshold optically pumped lasers with strain and dislocations management, optically pumped GeSn lasers that can be wavelength tuned by strain and lase up to room temperature, mid-IR photodetectors at room temperature, and the first electrically pumped GeSn laser at cryogenic temperatures. The performance of GeSn lasers continues to improve rapidly, the main challenges nowadays being continuous-wave electrical pumping, low lasing thresholds, higher temperature operation and reasonable wall plug efficiencies.

CRediT authorship contribution statement

Vincent Reboud: Conceptualization, Investigation, Methodology, Supervision, Writing – original draft, Writing – review & editing. **Omar Concepción:** Formal analysis, Investigation, Methodology, Writing – original draft. **Wei Du:** Conceptualization, Formal analysis, Investigation, Writing – original draft. **Moustafa El Kurdi:** Conceptualization, Formal analysis, Investigation, Methodology, Writing – original draft. **Jean Michel Hartmann:** Conceptualization, Formal analysis, Investigation, Writing – original draft. **Zoran Ikonic:** Formal analysis, Investigation. **Simone Assali:** Investigation, Writing – review & editing. **Nicolas Pauc:** Conceptualization, Formal analysis, Investigation, Methodology, Writing – original draft. **Vincent Calvo:** Formal analysis, Investigation, Methodology. **Clément Cardoux:** Formal analysis, Investigation, Methodology. **Eric Kroemer:** Formal analysis, Investigation, Methodology. **Nicolas Coudurier:** Formal analysis, Investigation, Methodology. **Philippe Rodriguez:** Formal analysis, Funding acquisition, Methodology, Writing – original draft. **Fisher Yu:** Formal analysis, Investigation, Methodology, Writing – review & editing. **Dan Buca:** Data curation, Investigation, Methodology, Writing – review & editing. **Alexei Chelnokov**: Data curation, Investigation, Methodology, Writing – review & editing.

Declaration of Competing Interest

The authors declare that they have no known competing financial interests or personal relationships that could have appeared to influence the work reported in this paper.

Data availability

Data will be made available on request.

Acknowledgment

We would like to acknowledge the scientific collaborators who have been working with us, in particular: Lara Casiez, Jérémie Chrétien, Marvin Frauenrath, Andrea Quintero, Quang M. Thai, Joris Aubin, Rami Khazaka, Alban Gassenq, Kevin Guilloy, Mathieu Bertrand, Stephan Wirths, Daniela Stange, Philippe Boucaud, Yann-Michel Niquet, Patrice Gergaud, Julie Widiez, Nicolas Bernier, Jérome Richy, Denis Rouchon, Frédéric Mazen, Pablo Acosta Alba, Oussama Moutanabbir, Guo-En Chang, Hans Sigg and Jerome Faist.

Some of the authors' work was supported by the European Union's Horizon 2020 LASTSTEP Project under the grant agreement ID: 101070208, the EDEN Carnot project and the CEA DRF-DRT Phare project. We gratefully acknowledge the clean room staff from Jülich, LETI and IRIG for their technical support.

References

[1] J.-M. Fedeli, S. Nicoletti, Mid-Infrared (Mid-IR) silicon-based photonics, Proc. IEEE 106 (12) (2018) 2302–2312.
[2] H. Lin, Z. Luo, T. Gu, L.C. Kimerling, K. Wada, A. Agarwal, J. Hu, Mid-infrared integrated photonics on silicon: a perspective, Nanophotonics 7 (2) (2018) 393–420, 2018.
[3] Y. Zou, S. Chakravarty, C.-J. Chung, X. Xu, Ray T. Chen, Mid-infrared silicon photonic waveguides and devices, Photon. Res. 6 (2018) 254–276.
[4] D. Grützmacher, O. Concepción, Q.T. Zhao, D. Buca, Si–Ge–Sn alloys grown by chemical vapour deposition: a versatile material for photonics, electronics, and thermoelectrics, Appl. Phys. A 129 (2023) 235.
[5] V. Reboud, D. Buca, H. Sigg, J.M. Hartmann, Z. Ikonic, N. Pauc, V. Calvo, P. Rodriguez, A. Chelnokov, Top. Appl. Phys. 139 (2021) 105–195.
[6] Y. Miao, G. Wang, Z. Kong, B. Xu, X. Zhao, X. Luo, H. Lin, Y. Dong, B. Lu, L. Dong, J. Zhou, J. Liu, H.H. Radamson, Review of Si-based GeSn CVD growth and optoelectronic applications, Nanomaterials 11 (2021) 2556.
[7] Y. Miao, G. Wang, Z. Kong, B. Xu, X. Zhao, X. Luo, H. Lin, Y. Dong, B. Lu, L. Dong, Review of Si-based GeSn CVD growth and optoelectronic applications, Nanomaterials 11 (2021) 2556.
[8] Y. Kim, S. Assali, D. Burt, Y. Jung, H.-J. Joo, M. Chen, Z. Ikonic, O. Moutanabbir, D. Nam, Enhanced GeSn microdisk lasers directly released on Si, Adv. Opt. Mater. 10 (2022) 2.
[9] M.R.M. Atalla, S. Assali, S. Koelling, A. Attiaoui, O. Moutanabbir, High-bandwidth extended-SWIR GeSn photodetectors on silicon achieving ultrafast broadband spectroscopic response, ACS Photonics 9 (4) (2022) 1425–1433, 2022.
[10] J. Aubin, J.M. Hartmann, GeSn growth kinetics in reduced pressure chemical vapor deposition from Ge2H6 and SnCl4, J. Cryst. Growth 482 (2018) 30–35.
[11] J. Chrétien, Q.M. Thai, M. Frauenrath, L. Casiez, A. Chelnokov, V. Reboud, J. M. Hartmann, M. El Kurdi, N. Pauc, V. Calvo, Room temperature optically pumped GeSn microdisk lasers, Appl. Phys. Lett. 120 (2022) 051107.
[12] O. Concepción, N.B. Søgaard, J.-H. Bae, Y. Yamamoto, A.T. Tiedemann, Z. Ikonic, G. Capellini, Q.-T. Zhao, D. Grützmacher, D. Buca, Isothermal heteroepitaxy of Ge1−xSnx structures for electronic and photonic applications, ACS Appl. Electron. Mater. 5 (4) (2023) 2268–2275.
[13] M. Frauenrath, V. Kiyek, N. von den Driesch, M. Veillerot, E. Nolot, D. Buca, J.-M. Hartmann, An in-depth study of the boron and phosphorous doping of GeSn, ECS J. Solid State Sci. Technol. 10 (2021) 085006.
[14] M. Frauenrath, O. Concepción, N. Gauthier, E. Nolot, D. Buca, J.-M. Hartmann, Advances in in situ boron and phosphorous doping of SiGeSn, ECS J. Solid State Sci. Technol. 12 (2023) 064001.
[15] J. Jiang, et al., Strain-induced enhancement of electroluminescence from highly strained germanium light-emitting diodes, ACS Photonics 6 (4) (2019) 915–923.
[16] S. Prucnal, et al., Ex situ n+ doping of GeSn alloys via non-equilibrium processing, Semicond. Sci. Technol. 33 (6) (2018) 065008.
[17] S. Prucnal, Ultra-doped n-type germanium thin films for sensing in the midinfrared, Sci. Rep. 6 (2016) 27643.
[18] L. Casiez, N. Bernier, J. Chrétien, J. Richy, D. Rouchon, M. Bertrand, F. Mazen, M. Frauenrath, A. Chelnokov, J.M. Hartmann, V. Calvo, N. Pauc, V. Reboud, P. Acosta Alba, Recrystallization of thick implanted GeSn layers with nanosecond laser annealing, J. Appl. Phys. 131 (2022) 153103.
[19] K. Takahashi, M. Kurosawa, H. Ikenoue, M. Sakashita, O. Nakatsuka, S. Zaima, High n-type Sb dopant activation in Ge-rich poly-Ge1−xSnx layers on SiO2 using pulsed laser annealing in flowing water, Appl. Phys. Lett. 112 (6) (2018) 062104.
[20] E. Galluccio, G. Mirabelli, A. Harvey, M. Conroy, E. Napolitani, R. Duffy, Cell formation in stanogermanides using pulsed laser thermal anneal on Ge0.91Sn0.09, Mater. Sci. Semicond. Process. 121 (2021) 105399.
[21] R. Chen, H. Lin, Y. Huo, C. Hitzman, T.I. Kamins, J.S. Harris, Structural and optical characterization of SixGe1−x−ySny alloys grown by molecular beam epitaxy, Appl. Phys. Lett. 99 (2011) 181125.
[22] J. Margetis, A. Mosleh, S. Al-Kabi, S.A. Ghetmiri, W. Du, W. Dou, M. Benamara, B. Li, M. Mortazavi, H.A. Naseem, S.Q. Yu, J. Tolle, Study of low-defect and strain-relaxed GeSn growth via reduced pressure CVD in H2 and N2 carrier gas, J. Cryst. Growth 463 (2017) 128.
[23] C.L. Senaratne, J.D. Gallagher, L. Jiang, T. Aoki, D.J. Smith, J. Menendez, J. Kouvetakis, Ge1-ySny (y = 0.01-0.10) alloys on Ge-buffered Si: Synthesis, microstructure, and optical properties, J. Appl. Phys. 116 (2014) 133509.
[24] J. Margetis, S.-Q. Yu, N. Bhargava, B. Li, W. Du, J. Tolle, Strain engineering in epitaxial Ge1−xSnx: a path towards low-defect and high Sn-content layers, Semicond. Sci. Technol. 32 (2017).
[25] S. Wirths, D. Buc, G. Mussler, A.T. Tiedemann, B. Holländer, P. Bernard, T. Stoica, D. Grützmacher, S. Mantl, Reduced pressure CVD growth of Ge and Ge 1−x Sn x alloys, ECS J. Solid State Sci. Technol. 2 (2013) 99–102.
[26] G. Abernathy, Y. Zhou, S. Ojo, B. Alharthi, P.C. Grant, W. Du, J. Margetis, J. Tolle, A. Kuchuk, B. Li, S.-Q. Yu, Study of SiGeSn/GeSn single quantum well towards high-performance all-group-IV optoelectronics, J. Appl. Phys. 129 (9) (2021) 093105.
[27] O. Olorunsola, S. Ojo, G. Abernathy, Y. Zhou, S. Amoah, P.C. Grant, W. Dou, J. Margetis, J. Tolle, A. Kuchuk, W. Du, B. Li, Y.-H. Zhang, S.-Q. Yu, Investigation of SiGeSn/GeSn single quantum well with enhanced well emission, Nanotechnology 33 (2021) 085201.
[28] G. Abernathy, S. Ojo, J.M. Grant, Y. Zhou, W. Du, A. Kuchuk, B. Li, S.-Q. Yu, Study of critical optical confinement factor for GeSn-based multiple quantum well lasers, Appl. Phys. Lett. 121 (2022) 171101.
[29] S. Wirths, R. Geiger, N. von den Driesch, G. Mussler, T. Stoca, S. Mantl, Z. Ikonic, M. Luysberg, S. Chiussi, J.M. Hartmann, H. Sigg, J. Faist, D. Buca, D. Grützmacher, Lasing in direct-bandgap GeSn alloy grown on Si, Nat. Photon 9 (2015) 88–92.
[30] Y. Zhou, S. Ojo, Y. Miao, H. Tran, J.M. Grant, G. Abernathy, S. Amoah, J. Bass, G. Salamo, W. Du, J. Liu, J. Margetis, J. Tolle, Y.-H. Zhang, G. Sun, R.A. Soref, B. Li, S.-Q. Yu, Electrically injected GeSn lasers with peak wavelength up to 2.7 micrometer at 90 K, Photon. Res 10 (2022) 222–229.
[31] B. Marzban, L. Seidel, T. Liu, K. Wu, V. Kiyek, M.Hartwig Zoellner, Z. Ikonic, J. Schulze, D. Grützmacher, G. Capellini, M. Oehme, J. Witzens, D. Buca, Strain engineered electrically pumped SiGeSn microring lasers on Si, ACS Photonics 10 (1) (2023) 217–224.
[32] A. Elbaz, R. Arefin, E. Sakat, B. Wang, E. Herth, G. Patriarche, A. Foti, R. Ossikovski, S. Sauvage, X. Checoury, K. Pantzas, I. Sagnes, J. Chrétien, L. Casiez, M. Bertrand, V. Calvo, N. Pauc, A. Chelnokov, P. Boucaud, F. Boeuf, V. Reboud, J.-M. Hartmann, M. El Kurdi, Reduced lasing thresholds in GeSn microdisk cavities with defect management of the optically active region, ACS Photonics 7 (10) (2020) 2713–2722.
[33] W. Du, Q.M. Thai, J. Chrétien, M. Bertrand, L. Casiez, Y. Zhou, J. Margetis, N. Pauc, A. Chelnokov, V. Reboud, V. Calvo, J. Tolle, B. Li, S.-Q. Yu, Study of si-based gesn optically pumped lasers with micro-disk and ridge waveguide structures, Front. Phys. 7 (2019) 147.
[34] Q.M. Thai, N. Pauc, J. Aubin, M. Bertrand, J. Chrétien, A. Chelnokov, J. M. Hartmann, V. Reboud, V. Calvo, 2D hexagonal photonic crystal GeSn laser with 16% Sn content, Appl. Phys. Lett. 113 (5) (2018) 051104.
[35] J. Chrétien, N. Pauc, F. Armand Pilon, M. Bertrand, Q.-M. Thai, L. Casiez, N. Bernier, H. Dansas, P. Gergaud, E. Delamadeleine, R. Khazaka, H. Sigg, J. Faist, A. Chelnokov, V. Reboud, J.-M. Hartmann, V. Calvo, GeSn lasers covering a wide wavelength range thanks to uniaxial tensile strain, ACS Photonics 6 (10) (2019) 2462–2469.
[36] B. Wang, E. Sakat, E. Herth, M. Gromovyi, A. Bjelajac, J. Chaste, G. Patriarche, P. Boucaud, F. Boeuf, N. Pauc, V. Calvo, J. Chrétien, M. Frauenrath, A. Chelnokov, V. Reboud, J.-M. Hartmann, M. El Kurdi, GeSnOI mid-infrared laser technology, Light Sci. Appl. 10 (2021) 232.
[37] M.P. Polak, P. Scharoch, R. Kudrawiec, The electronic band structure of Ge1−xSnx in the full composition range: indirect, direct, and inverted gaps regimes, band offsets, and the Burstein–Moss effect, J. Phys. D: Appl. Phys. 50 (2017) 195103.
[38] A. Bjelajac, M. Gromovyi, E. Sakat, B. Wang, G. Patriarche, N. Pauc, V. Calvo, P. Boucaud, F. Boeuf, A. Chelnokov, V. Reboud, M. Frauenrath, J.-M. Hartmann, and M. El Kurdi Up to 300 K lasing with GeSn-On-Insulator microdisk resonators 2022, 30, 3, 3954–3961.
[39] D. Buca, A. Bjelajac, D. Spirito, O. Concepción, M. Gromovyi, E. Sakat, X. Lafosse, L. Ferlazzo, N. von den Driesch, Z. Ikonic, D. Grützmacher, G. Capellini, M. El Kurdi, Room temperature lasing in GeSn microdisks enabled by strain engineering, Adv. Opt. Mater. 10 (22) (2022) 2201024.
[40] A. Quintero, P. Gergaud, J.-M. Hartmann, V. Reboud, Ph Rodriguez, Ni-based metallization of GeSn layers: a review and recent advances, Microelectron. Eng. 269 (2023) 111919.
[41] G. Han, S. Su, C. Zhan, Q. Zhou, Y. Yang, L. Wang, P. Guo, W. Wei, C.P. Wong, Z. X. Shen, B. Cheng, Y.C. Yeo, High-mobility germanium-tin (GeSn) P-channel MOSFETs featuring metallic source/drain and sub-370 °C process modules, 2011 Int. Electron Devices Meet. (IEDM) (2011) 16.7.1–16.7.3.
[42] Y. Liu, H. Wang, J. Yan, G. Han, Reduction of formation temperature of nickel monostanogermanide [Ni(GeSn)] by the incorporation of tin, ECS Solid State Lett. 3 (2) (2014) P11–P13.
[43] S. Wirths, R. Troitsch, G. Mussler, P. Zaumseil, J.-M. Hartmann, T. Schroeder, S. Mantl, D. Buca, Ni(SiGeSn) metal contact formation on low bandgap strained (Si)Ge(Sn) semiconductors, ECS Trans. 64 (6) (2014) 107–112.
[44] A. Quintero, P. Gergaud, J. Aubin, J.-M. Hartmann, V. Reboud, Ph Rodriguez, "Ni / GeSn solid-state reaction monitored by combined X-ray diffraction analyses: Focus on the Ni-rich phase, J. Appl. Cryst. 51 (4) (2018) 1133–1140.
[45] T. Nishimura, O. Nakatsuka, Y. Shimura, S. Takeuchi, B. Vincent, A. Vantomme, J. Dekoster, M. Caymax, R. Loo, S. Zaima, Formation of Ni(Ge1−xSnx) layers with solid phase reaction in Ni/Ge1−xSnx/Ge systems, Solid-State Electron. 60 (1) (2011) 46–52.
[46] A. Quintero, P. Gergaud, J.-M. Hartmann, V. Delaye, V. Reboud, E. Cassan, Ph Rodriguez, Impact and behavior of Sn during the Ni/GeSn solid-state reaction, J. Appl. Cryst. 53 (3) (2020) 605–613.
[47] N. Coudurier, A. Quintero, V. Loup, P. Gergaud, J.-M. Hartmann, D. Mariolle, V. Reboud, Ph Rodriguez, Plasma surface treatment of GeSn layers and its subsequent impact on Ni / GeSn solid-state reaction, Microelectron. Eng. 257 (2022) 111737.
[48] A. Quintero, P. Gergaud, J.-M. Hartmann, V. Reboud, E. Cassan, Ph Rodriguez, Impact of alloying elements (Co, Pt) on nickel stanogermanide formation, Mater. Sci. Semicond. Process. 108 (2020) 104890.
[49] A. Quintero, P. Gergaud, J. Aubin, J.M. Hartmann, N. Chevalier, J.P. Barnes, V. Loup, V. Reboud, F. Nemouchi, Ph Rodriguez, Impact of Pt on the phase formation sequence, morphology, and electrical properties of Ni(Pt)/Ge0.9Sn0.1 system during solid-state reaction, J. Appl. Phys. 124 (8) (2018) 085305.
[50] Q. Liu, W. Geilei, Y. Guo, X. Ke, H. Radamson, H. Liu, C. Zhao, J. Luo, Improvement of the thermal stability of nickel stanogermanide by carbon pre-stanogermanidation implant into GeSn substrate, ECS J. Solid State Sci. Technol. 4 (3) (2015) P67–P70.
[51] A. Quintero, F. Mazen, P. Gergaud, N. Bernier, J.-M. Hartmann, V. Reboud, E. Cassan, Ph Rodriguez, Enhanced thermal stability of Ni/GeSn system using pre-amorphization by implantation, J. Appl. Phys. 129 (11) (2021) 15302.

[52] Y. Wu, H. Xu, K. Han, X. Gong, Thermal stability and Sn segregation of low-resistance Ti/p+-Ge0.95Sn0.05 contact, IEEE Electron Device Lett. vol. 40 (10) (2019) 1575–1578.

[53] A. Quintero, P. Gergaud, J.-M. Hartmann, V. Reboud, E. Cassan, P. Rodriguez, Impact of Sn on the Ti/Ge solid-state reaction: Phase formation sequence, morphological and electrical properties, Microelectron. Eng. 252 (2022) 111667.

[54] E. Galluccio, G. Mirabelli, A. Harvey, M. Conroy, E. Napolitani, R. Duffy, Cell formation in stanogermanides using pulsed laser thermal anneal on Ge0.91Sn0.09, Mater. Sci. Semicond. Process. 121 (2021) 105399.

[55] A. Quintero, P.A. Alba, J.-M. Hartmann, P. Gergaud, V. Reboud, and Ph Rodriguez, "Innovative annealing technology for thermally stable Ni(GeSn) alloys," in 21st International Workshop on Junction Technology (IWJT-2023).

[56] H.H. Tseng, K.Y. Wu, H. Li, V. Mashanov, H.H. Cheng, G. Sun, R.A. Soref, Mid-infrared electroluminescence from a Ge/$Ge_{0.922}Sn_{0.078}$/Ge double heterostructure p-i-n diode on a Si substrate, Appl. Phys. Lett. 102 (2013) 182106.

[57] Y. Zhou, W. Dou, W. Du, T. Pham, S.A. Ghetmiri, S. Al-Kabi, A. Mosleh, M. Alher, J. Margetis, J. Tolle, G. Sun, R. Soref, B. Li, M. Mortazavi, H. Naseem, S.-Q. Yu, Systematic study of GeSn heterostructure-based light-emitting diodes towards midinfrared applications, J. Appl. Phys. 120 (2016) 023102.

[58] L.-F. Zhang, B. Shu, R.-H. Jiang, Y.-L. Gao, H.-M. Zhang, R.-X. Xuan, H.-Y. Hu, Short wave infrared LEDs based on strained GeSn, 2018, Microw. Opt. Technol. Lett. 60 (5) (2018) 1151–1154.

[59] B.-J. Huang, C.-Y. Chang, Y.-D. Hsieh, R.A. Soref, G. Sun, H.-H. Cheng, G.-E. Chang, Electrically injected GeSn vertical-cavity surface emitters on silicon-on-insulator platforms, ACS Photonics 6 (2019) 1931–1938.

[60] M.R.M. Atalla, S. Assali, G. Daligou, A. Attiaoui, S. Koelling, P. Daoust, and O. Moutanabbir, Continuous-wave GeSn light emitting diodes on silicon with 2.5 µm room-temperature emission, arXiv:2310.00225 [physics.optics], https://doi.org/10.48550/arXiv.2310.00225.

[61] M. Bertrand, N. Pauc, Q.M. Thai, J. Chrétien, L. Casiez, A. Quintero, Ph Rodriguez, R. Khazaka, J. Aubin, J.-M. Hartmann, A. Chelnokov, V. Calvo, V. Reboud, Mid-infrared GeSn-based LEDs with Sn content up to 16%, IEEE 16th International Conference on Group IV Photonics, GFP-2019, 2019 1949–209×1–2. 10.1109/GROUP4.2019.8853926.

[62] C. Cardoux, L. Casiez, N. Pauc, V. Calvo, N. Coudurier, P. Rodriguez, J. Richy, P. Barritault, O. Lartigue, C. Constancias, M. Frauenrath, J.M. Hartmann, A. Chelnokov, O. Gravrand, V. Reboud, Room temperature spectral characterization of direct band gap Ge0.85Sn0.15 LEDs and photodiodes, 2022 12006, Silicon Photonics XVII; 120060A.

[63] L. Casiez, M. Bertrand, J. Chretien, A. Quintero, Q.M. Thai, M. Frauenrath, O. Lartigue, P. Barritault, N. Bernier, P. Rodriguez, A. Chelnokov, J.-M. Hartmann, N. Pauc, V. Calvo, V. Reboud, GeSn heterostructures LEDs for gas detection (Vancouver, BC, Canada), IEEE Photonics Conf. (IPC) (2020) 1–2.

[64] B. Schwartz, M. Oehme, K. Kostecki, D. Widmann, M. Gollhofer, R. Koerner, S. Bechler, I.A. Fischer, T. Wendav, E. Kasper, J. Schulze, M. Kittler, Electroluminescence of GeSn/Ge MQW LEDs on Si substrate, Opt. Lett. 40 (2015) 3209–3212.

[65] M. Oehme, M. Gollhofer, D. Widmann, M. Schmid, M. Kaschel, E. Kasper, J. Schulze, Direct bandgap narrowing in Ge LED's on Si substrates, Opt. Express 21 (2) (2013) 2206–2211.

[66] D. Stange, N. von den Driesch, D. Rainko, S. Roesgaard, I. Povstugar, J.-M. Hartmann, T. Stoica, Z. Ikonic, S. Mantl, D. Grützmacher, D. Buca, Short-wave infrared LEDs from GeSn/SiGeSn multiple quantum wells, Optica 4 (2) (2017) 185–188.

[67] L. Peng, X. Li, J. Zheng, X. Liu, M. Li, Z. Liu, C. Xue, Y. Zuo, B. Cheng, Room-temperature direct-bandgap electroluminescence from type-I GeSn/SiGeSn multiple quantum wells for 2 µm LEDs, J. Lumin. 228 (2020) 117539.

[68] W. Du, Y. Zhou, S.A. Ghetmiri, A. Mosleh, B.R. Conley, A. Nazzal, R.A. Soref, G. Sun, J. Tolle, J. Margetis, H.A. Naseem, S.-Q. Yu, Room-temperature electroluminescence from Ge/Ge1-xSnx/Ge diodes on Si substrates, Appl. Phys. Lett. 104 (2014) 241110.

[69] S. Wu, L. Zhang, R. Wan, H. Zhou, K.H. Lee, Q. Chen, Y.-C. Huang, X. Gong, C. S. Tan, Ge0.92Sn0.08/Ge multi-quantum-well LEDs operated at 2-µm-wavelength on a 12-inch Si substrate, Photonics Res. 11 (10) (2023) 1606–1612.

[70] Q. Chen, Y. Jung, H. Zhou, S. Wu, X. Gong, Y.-C. Huang, K.H. Lee, L. Zhang, D. Nam, J. Liu, J.-W. Luo, W. Fan, C.S. Tan, GeSn/Ge Multiquantum-Well Vertical-Cavity Surface-Emitting p-i-n Structures and Diode Emitters on a 200 mm Ge-on-Insulator Platform, ACS Photonics 10 (2023) 1716.

[71] J. Margetis, S. Al-Kabi, W. Du, W. Dou, Y. Zhou, T. Pham, P. Grant, S. Ghetmiri, A. Mosleh, B. Li, J. Liu, G. Sun, R. Soref, J. Tolle, M. Mortazavi, S.-Q. Yu, Si-based GeSn lasers with wavelength coverage of 2–3 µm and operating temperatures up to 180 K, ACS Photonics 5 (2017) 827–833.

[72] Q. Thai, N. Pauc, J. Aubin, M. Bertrand, J. Chrétien, V. Delaye, A. Chelnokov, J. Hartmann, V. Reboud, V. Calvo, GeSn heterostructure micro-disk laser operating at 230 K, Opt. Express 26 (2018) 32500–32508.

[73] Y. Zhou, W. Dou, W. Du, S. Ojo, H. Tran, S. Ghetmiri, J. Liu, G. Sun, R. Soref, J. Margetis, J. Tolle, B. Li, Z. Chen, M. Mortazavi, S.-Q. Yu, Optically Pumped GeSn Lasers Operating at 270 K with Broad Waveguide Structures on Si, ACS Photonics 6 (2019) 1434–1441.

[74] A. Elbaz, D. Buca, N. von den Driesch, K. Pantzas, G. Patriarche, N. Zerounian, E. Herth, X. Checoury, S. Sauvage, I. Sagnes, A. Foti, R. Ossikovski, J. Hartmann, F. Boeuf, Z. Ikonic, P. Boucaud, D. Grützmacher, M. El Kurdi, Ultra-low threshold cw and pulsed lasing in tensile strained GeSn alloys, Nat. Photon 14 (2020) 375–382.

[75] Y. Zhou, Y. Miao, S. Ojo, H. Tran, G. Abernathy, J.M. Grant, S. Amoah, G. Salamo, W. Du, J. Liu, J. Margetis, J. Tolle, Y.-H. Zhang, G. Sun, R.A. Soref, B. Li, S.-Q. Yu, Electrically injected GeSn lasers on Si operating up to 100 K, Optica 7 (2020) 924–928.

[76] Y. Zhou, S. Ojo, C.-W. Wu, Y. Miao, H. Tran, J.M. Grant, G. Abernathy, S. Amoah, J. Bass, G. Salamo, W. Du, G.-E. Chang, J. Liu, J. Margetis, J. Tolle, Y.-H. Zhang, G. Sun, R.A. Soref, B. Li, S.-Q. Yu, Electrically injected GeSn lasers with peak wavelength up to 2.7 µm, Photon. Res. 10 (2022) 222–229.

[77] B.R. Conley, J. Margetis, W. Du, H. Tran, A. Mosleh, S.A. Ghetmiri, J. Tolle, G. Sun, R. Soref, B. Li, et al., Si based GeSn photoconductors with a 1.63 A/W peak responsivity and a 2.4 µm long-wavelength cutoff, Appl. Phys. Lett. 105 (2014) 221117.

[78] T.N. Pham, W. Du, B.R. Conley, J. Margetis, G. Sun, R.A. Soref, J. Tolle, B. Li, S. Q. Yu, Si-based Ge0.9Sn0.1 photodetector with peak responsivity of 2.85 A/W and longwave cutoff at 2.4 µm, Electron. Lett. 51 (2015) 854–856.

[79] A. Gassenq, F. Gencarelli, J. Van Campenhout, Y. Shimura, R. Loo, G. Narcy, B. Vincent, G. Roelkens, GeSn/Ge heterostructure short-wave infrared photodetectors on silicon, Opt. Express 20 (2012) 27297–27303.

[80] H. Tran, T. Pham, J. Margetis, Y. Zhou, W. Dou, P.C. Grant, J. Grant, G. Sun, J. Tolle, W. Du, et al., Si-based GeSn photodetectors toward mid-infrared imaging applications, ACS Photonics 6 (2019) 2807–2815.

[81] M.R.M. Atalla, S. Assali, A. Attiaoui, C. Lemieux-Leduc, A. Kumar, S. Abdi, O. Moutanabbir, All-Group IV Transferable Membrane Mid-Infrared Photodetectors, Adv. Funct. Mater. 31 (2021) 2006329.

[82] J. Mathews, R. Roucka, J. Xie, S.Q. Yu, J. Menéndez, J. Kouvetakis, Extended performance GeSn/Si (100) p-i-n photodetectors for full spectral range telecommunication applications, Appl. Phys. Lett. 95 (2009) 133506.

[83] E.T. Simola, V. Kiyek, A. Ballabio, V. Schlykow, J. Frigerio, C. Zucchetti, A. De Iacovo, L. Colace, Y. Yamamoto, G. Capellini, D. Grützmacher, D. Buca, G. Isella, CMOS-Compatible Bias-Tunable Dual-Band Detector Based on GeSn/Ge/Si Coupled Photodiodes, ACS Photonics 8 (2021) 2166–2173.

[84] M.R.M. Atalla, S., S. Koelling, A. Attiaoui, O. Moutanabbir, High-Bandwidth Extended-SWIR GeSn Photodetectors on Silicon Achieving Ultrafast Broadband Spectroscopic Response, ACS Photonics 9 (2022) 1425–1433.

[85] H. Zhou, S. Xu, S. Wu, Y.C. Huang, P. Zhao, J. Tong, B. Son, X. Guo, D. Zhang, X. Gong, et al., Photodetection and modulation from 1550 to 2000 nm realized by a GeSn/Ge multiple-quantum-well photodiode on a 300-mm Si substrate, Opt. Express 28 (2020) 34772–34786.

[86] S. Wu, S. Xu, H. Zhou, Y. Jin, Q. Chen, Y.C. Huang, L. Zhang, X. Gong, C.S. Tan, High-performance back-illuminated Ge0.92Sn0.08/Ge multiple-quantum-well photodetector on Si platform for SWIR Detection, IEEE J. Sel. Top. Quantum Electron. 28 (2021) 1–9.

[87] H. Zhou, S. Xu, Y. Lin, Y.C. Huang, B. Son, Q. Chen, X. Guo, K. Lee, S. Goh, X. Gong, et al., High-efficiency GeSn/Ge multiplequantum- well photodetectors with photon-trapping microstructures operating at 2 µm, Opt. Express 28 (2020) 10280–10293.

[88] Q. Chen, H. Zhou, S. Xu, Y.-C. Huang, S. Wu, K.H. Lee, X. Gong, C.S. Tan, A Route toward High-Detectivity and Low- Cost Short-Wave Infrared Photodetection:GeSn/Ge Multiple-Quantum-Well Photodetectors with a Dielectric Nanohole Array Metasurface, ACS Nano 17 (2023) 12151–12159.

[89] X. Li, L. Peng, Z. Liu, Z. Zhou, J. Zheng, C. Xue, Y. Zuo, B. Chen, B. Cheng, 30 GHz GeSn photodetector on SOI substrate for 2 µm wavelength application 2021, 9, 4, 494–500.

[90] C. Cardoux, L. Casiez, M. Frauenrath, N. Pauc, V. Calvo, J.M. Hartmann, N. Coudurier, et al., Direct Band Gap Ge0.85Sn0.15 Photodiodes For Room Temperature Gas Sensing, IEEE Int. Conf. Group IV Photonics GFP (2023), https://doi.org/10.1109/SiPhotonics55903.2023.10141903.